Master's Thesis
석사 학위논문

Development of Organic Semiconductors for Soft Electronics

Seong Hoon Yu(유 성 훈 兪 性 勳)

Department of
Energy Science & Engineering

DGIST

2020

Master's Thesis
석사 학위논문

Development of Organic Semiconductors for Soft Electronics

Seong Hoon Yu(유 성 훈 兪 性 勳)

Department of

Energy Science & Engineering

DGIST

2020

Development of Organic Semiconductors for Soft Electronics

Advisor: Professor Jiwoong Yang
Co-advisor: Professor Jongmin Choi

by

Seong Hoon Yu
Department of Energy Science & Engineering
DGIST

A thesis submitted to the faculty of DGIST in partial fulfillment of the requirements for the degree of Master of Science in the Department of Energy Science & Engineering. The study was conducted in accordance with Code of Research Ethics[1]

05. 08. 2020

Approved by

Professor Jiwoong Yang   (signature)
(Advisor)

Professor Jongmin Choi   (signature)
(Co-Advisor)

---

[1] Declaration of Ethical Conduct in Research: I, as a graduate student of DGIST, hereby declare that I have not committed any acts that may damage the credibility of my research. These include, but are not limited to: falsification, thesis written by someone else, distortion of research findings or plagiarism. I affirm that my thesis contains honest conclusions based on my own careful research under the guidance of my thesis advisor.

Development of Organic Semiconductors for Soft Electronics

Seong Hoon Yu

Accepted in partial fulfillment of the requirements for the degree of Master of Science.

05. 08. 2020

Head of Committee   Prof. Jiwoong Yang (signature)

Committee Member   Prof. Jongmin Choi (signature)

Committee Member   Prof. Ju Hyuck Lee (signature)

MS/ES
201744002

유 성 훈. Seong Hoon Yu. Development of Organic Semiconductors for Soft Electronics. Department of Energy Science & Engineering. 2020. 56p. Advisors Prof. Jiwoong Yang, Co-Advisors Prof. Jongmin Choi

ABSTRACT

Organic semiconductor based soft electronic devices are demonstrated: (1) effects of conjugation length on charge transport in polymer semiconductors, (2) water-borne colloids of organic semiconductors, and (3) breath-figure molding of polymer semiconductors for sensors.

To improve the charge carrier mobility of diketopyrrolopyrrole donor-acceptor copolymer semiconductors, the length of the donor building block is controlled using vinylene moieties, and its effects on crystalline structure and charge transport are systematically studied. We synthesize P29-DPP-TBT with two vinylene linkages between thiophene units and compare it with P29-DPP-TVT with single vinylene linkage. Density functional theory calculations predict enhanced backbone planarity of P29-DPP-TBT compared to P29-DPP-TVT, which can be related with the increased conjugation length of P29-DPP-TBT as proved by the increased free exciton bandwidth extracted from UV-vis absorption spectra and the wavenumber shift of the C–C peaks to higher values in Raman spectra. From two-dimensional grazing incident X-ray diffraction studies, it is turned out that the paracrystalline disorder is lower in P29-DPP-TBT than in P29-DPP-TVT. Near-edge X-ray absorption fine structure spectroscopy reveal that more edge-on structure of polymer backbone is formed in the case of P29-DPP-TBT. By measuring the temperature-dependence of the charge carrier mobilities, it is turned out that the activation energy for charge hopping is lower for P29-DPP-TBT than for P29-DPP-TVT. Collectively, these results imply that the substitution of extended π-conjugated donor moiety of polymeric semiconductors can yield a more planar backbone structure and thus enhanced intermolecular interaction which enables more perfect crystalline structure as well as enhanced charge transport behavior.

A synthetic approach has demonstrated to enhance coalescence phenomenon during solidification of water-borne colloids so that thin, even, and continuous film morphology of polymer semiconductors can be realized. From theoretical study of complex colloids, it is shown that small-sized and uniform colloid particles

are essential to minimize depletion contact energy between colloid particles and thus to enhance coalescence. Therefore, the newly synthesized polymer semiconductor is designed for better molecular affinity with surfactants, so that phase transfer of polymer semiconductors from organic phase to water phase can proceed more efficiently during mini-emulsion synthesis. This is achieved by substituting a Si atom to the branching C atom of the alkyl solubilizing group of a conventional donor-acceptor polymer semiconductor. Such a chemical modification increases the volumetric portion of hydrophobic alkyl chains and thus enables higher solubility as well as higher hydrophobicity, all of which are closely related with enhancing molecular affinity between polymer semiconductor and surfactants. As a result, the performance of organic field-effect transistors fabricated from water-borne colloids can be improved to a level similar to the case of organic solvents. More importantly, the reproducibility of transistor performance is also greatly improved due to the small and uniform water-borne colloidal particles.

Strategically designed polymer semiconductor thin film morphology with both high responsivity to the specific gas analyte and high signal transport efficiency is reported to realize high-performance flexible NO_x gas sensors. Breath-Figure (BF) molding of polymer semiconductors enables a finely defined degree of nanoporosity in polymer films with high reproducibility while maintaining a high charge carrier mobility characteristics of organic field effect transistors (OFETs). The optimized BF-OFET with a donor-acceptor copolymer exhibits a maximum responsivity of over 10^4%, sensitivity of 774%/ppm, and limit of detection (LOD) of 110 ppb against NO. When tested across at NO concentrations of 0.2–10 ppm, the BF-OFET gas sensor exhibits a response time of 100–300 s, which is suitable for safety purposes in practical applications. Furthermore, BF-OFETs show a high reproducibility as confirmed by statistical analysis on 64 independently fabricated devices. Selectivity to NO_x analytes is tested by comparing the sensing ability of BF-OFET to other reducing gases and volatile organic compounds. Finally, flexible BF-OFETs conjugated with plastic substrates are demonstrated and they exhibit a sensitivity of 500%/ppm and LOD of 215 ppb, with a responsivity degradation of only 14.2% after 10,000 bending cycle at 1% strain.

List of Contents

Part 1. Effects of conjugation length on crystalline perfectness and charge transport in diketopyrrolopyrrole-based polymer semiconductors

Part 2. Facilitating Phase Transfer of Polymer Semiconductor in Mini-Emulsion Synthesis via Molecular Affinity Engineering

List of Tables

List of Figures

profiles along (e) with q_z direction and (f) q_{xy} direction. The pole figures for each film normalized by (200) scattered intensity (g) with DPP-TVT film and (h) with SiDPP-TVT film.

Figure 2.5 The transfer curves of (a) chloroform based devices and (b) water based devices. (c) The output characteristics of water based devices using SiDPP-TVT. (d) Device-to-device deviation of charge carrier mobility comparison in DPP-TVT and SiDPP-TVT using mini-emulsion synthesis.

Part 3.

Figure 3.1 (a) Polymer semiconductor selection criteria for high-performance OSC gas sensor, and the chemical structures of the polymer semiconductors used in this study. (b) The scheme of BF molding of polymer semiconductor films and final device structure. (c–f) The top row shows SEM top-view images of the fabricated polymer films, the middle row shows the corresponding AFM topographical images, and the bottom row shows the corresponding GIXD patterns. From the left, polymer films corresponding to these images are pristine, BF-S, BF-M, and BF-L DPP-DTT, respectively. (g) Pore size distribution of each BF molding film. (h) Line cut profiles extracted from AFM images to confirm actual pore size and height. (i) Transfer curves of pristine, BF-S, BF-M, and BF-L films exposed to N_2. (j) Responsivities of BF molding devices calculated from transfer curves corresponding to N_2 and 10 ppm NO exposure. The shaded region indicates a V_{GS} below V_{th}.

Figure 3.2 Transfer curves of (a) BF-S, (b) BF-M, and (c) BF-L at different time periods after exposure to 10 ppm NO. Recovery states of (d) BF-S, (e) BF-M, and (f) BF-L under N_2 purging.

Figure 3.3 Changes in the transfer curves at NO gas concentrations of (a) 0.2, (b) 0.5 and (c) 1 ppm, respectively. (d) Responsivities at various NO gas concentrations calculated from transfer curves corresponding to N_2 and NO gas exposure. The shaded region indicates a V_{GS} below V_{th}. (e) Threshold voltage shift with gas exposure time at various NO concentrations. (f) Transient response at 0.2–3 ppm NO at $V_{GS} = -15$ V and $V_{DS} = -30$ V. (g) Corresponding its responsivity and calculation of its sensitivity and LOD. (h) Normalized response at NO concentrations of 0.5–10 ppm. (i) Responsivity distribution upon exposure of 64 independently fabricated devices to 3 ppm NO. (j) Responsivity of the sensor to upon exposure to different gases (concentration below 10 ppm). The bias condition is the same as that used for transient response measurements.

Figure 3.4 (a) Changes in the transfer curves of flexible sensors upon exposure to 10 ppm NO. (b) Transfer curves after bending the sensor (radius: 6.3 mm, strain: 1%) for 0–10000 times. (c) Responsivity changes after bending the sensor for 0–10000 times and exposing it to 3 ppm NO. The photo shows the actual bending test and radius of curvature. (d) Transient response of the flexible sensor upon exposure to 0.5–3 ppm NO at $V_{GS} = -8$ V and $V_{DS} = -30$ V. The inset image is actual flexible device. (e) Corresponding its responsivity and calculation of its sensitivity and LOD. The bias condition is the same as that used for transient response measurements.

Part 1. Effects of conjugation length on crystalline perfectness and charge transport in diketopyrrolopyrrole-based polymer semiconductors

I. Introduction

Solution-processable organic field-effect transistors (FETs) based on organic semiconductors have attracted considerable attention owing to their potential use in low-cost, flexible electronic devices for various applications, such as sensors, e-papers, and backplanes of organic light-emitting diode displays.[1-5] Among the various organic semiconductors, conjugated polymers are considered the most promising candidates for next-generation organic semiconductors owing to their outstanding solution processability, mechanical robustness, and reproducibility, and thus are being actively developed.[6-8] With continuous development of conjugated polymer field-effect transistors (PFETs), the charge carrier mobility of amorphous Si (0.5–1 cm^2 V^{-1} s^{-1}) has been surpassed.[9-11] As part of this effort, structural control of conjugated polymers by changing their molecular units has been studied in combination with molecular physics, with the aim of rationalizing the design of new materials with high charge carrier mobilities. Novel high-performance polymer semiconductors have been designed and synthesized with improved chain alignment, backbone planarity, and degrees of crystallinity.[12-16] For example, a molecular design widely used in the design of conjugated polymers uses an electron donor and an electron acceptor to effectively improve intermolecular interactions and intramolecular charge transfer. Various donor–acceptor building blocks have been devised to synthesize highly planar copolymers with high charge carrier mobilities, including diketopyrrolopyrrole (DPP),[12,13] isoindigo,[14] naphthalene diimide,[15] and benzobisthiadiazole.[16]

Recently, it has been discovered that the key to designing high-mobility polymers for enhancing the efficiency of intramolecular charge transfer, is not enhancing the degree of crystallinity, but increasing introspection to inevitably large amounts of disorder in aggregates, which is related to paracrystalline disorder.[17, 18] In other words, to further enhance the charge transport nature of donor-acceptor copolymers, the degree of crystalline aggregation and the degree of paracrystalline disorder play very important roles. In a previous study, we optimized the alkyl spacer length of a DPP polymer to improve the donor-acceptor copolymer structure.[19] However, in polymer structure design, optimization of the donor portion of the copolymer for efficient intramolecular charge transfer is also very important, and microscopic changes can have a large influence on charge transfer. While varying the alkyl spacer length of the molecular unit is straightforward, changing the donor structure to achieve optimal donor-acceptor interaction in a copolymer requires very sophisticated engineering. It is difficult to predict how changes in the donor moiety will influence charge transport. Therefore,

we investigated the effect of the degree of conjugation of a donor moiety on the crystalline structure and charge transport properties of a copolymer by synthesizing a new polymer called diketopyrrolopyrrole-thiophene-butadiene-thiophene (DPP-TBT), and conducting comparative studies with diketopyrrolopyrrole-thiophene-vinylene-thiophene (DPP-TVT), which was reported previously.[19] We found that the addition of a single vinylene group to the donor moiety can dramatically improve charge transport owing to increased conjugation length, increased backbone planarity, and reduced structural disorder. We characterized the new polymer using various techniques, such as UV-vis absorption spectroscopy, Raman spectroscopy, two-dimensional grazing incidence X-ray diffraction (2-D GIXD), near edge X-ray absorption fine structure spectroscopy (NEXAFS), and atomic force microscopy (AFM), as well as density functional theory (DFT) calculations. Furthermore, we conducted temperature dependent thin film transistor measurements. For precise measurements of the charge transport nature of the polymer, we fabricated FET devices using a high capacitance ZrO_2 layer as a thin dielectric, which prevented the kink effect in charge transport measurements.[20]

II. Experimental Section

2.1 Materials

All solvents and reagents were purchased from Aldrich, Alfa Aesar, or TCI. Catalysts used in coupling reactions were purchased from UMICORE. P29-DPP-Br was prepared using literature methods.[12] All other materials were of a common commercial level and were used as received. All solvents used were purified prior to use.

2.2 Device fabrication

A bare Si wafer was used as the substrate, and a ZrO_2 sol-gel method was used to fabricate a thin ZrO_2 dielectric layer following the previously reported method.[21] To make the ZrO_2 dielectric layer more hydrophobic and electrically robust, an octadecylphosphonic acid (ODPA) self-assembled monolayer was deposited by im-

mersion.[22] The active layer was completed by spin-coating solutions of P29-DPP-TVT or P29-DPP-TBT in chloroform (0.5 wt%) onto the ZrO$_2$/ODPA-treated substrate. To further enhance molecular order between the DPP molecules, the prepared films were annealed at different temperatures (100 °C–200 °C) for 20 min and then cooled slowly. Finally, the PFET geometry was completed by depositing Au source-drain electrodes onto the annealed films.

2.3 Characterization

2-D GIXD measurements were performed using the PLS-II 3C beamline at the Pohang Accelerator Laboratory (PAL) in Korea. All NEXAFS measurements were performed at room temperature at the 4D beamline of the Pohang Light Source II (PLSII). We used the partial-electron-yield detection mode for NEXAFS spectra by recording the sample current normalized to a signal current measured simultaneously using a Au mesh under an ultrahigh vacuum. We used a p-polarized synchrotron photon beam (~85 %) with an energy of 279-325 eV, a spectral energy resolution of $\Delta E = 150$ meV, and a ~5 nm probing depth for surface-sensitive measurements. For these X-ray measurements, polymer films were obtained by spin-coating each polymer on the Si/ZrO$_2$/ODPA substrate, followed by thermal annealing at 200 °C for 20 minutes, consistent with the device fabrication conditions. All morphological images were obtained using an atomic force microscope (Park systems, NX20).

2.4 Measurements

^{1}H-NMR and ^{13}C-NMR spectra were recorded using Bruker Avance-300 and DRX-500 MHz spectrometers. Thermal analysis was performed on a TA Instruments TGA 2100 thermogravimetric analyzer in a nitrogen atmosphere at a rate of 10 °C min^{-1}. Differential scanning calorimetry (DSC) was conducted under nitrogen on a TA Instruments 2100 differential scanning calorimeter, with the sample heated at 10 °C min^{-1} from 30 to 300 °C. Molecular weights and polydispersities of the copolymers were determined by gel permeation chromatography analysis with a polystyrene standard calibration (Waters high-pressure gel permeation chromatography assembled with a model M515 pump, μ-Styragel columns (HR4, HR4E, and HR5E), with 500 and 100 Å resolution, refractive index detectors, and chloroform as solvent). Cyclic voltammetry (CV) was performed using an EG&G PAR model 273A" potentiostat/galvanostat with three-electrode cells in a solution of 0.1 M tetrabutylammonium perchlorate (Bu4NClO4) in acetonitrile at a scan rate of 50 mV s^{-1}. The polymer films were coated on a square carbon electrode by dipping the electrode into the corresponding solvents and then drying nitro-

gen. A Pt wire was used as the counter electrode, and a $Ag/AgNO_3$ (0.1 M) electrode was used as the reference electrode. UV−vis absorption spectra were measured using a UV-1650PC spectrophotometer. Raman spectra were measured using a Renishaw inVia Raman spectrometer equipped with a 785 nm diode laser. DFT calculations were carried out with Gaussian computational programs. The capacitance values of the dielectric layers were measured using a Keysight E4981 capacitance meter at 1 kHz. The capacitance of the ZrO_2/ODPA layer was 3.5×10^{-7} F cm^{-2} at 1 kHz. Contact-angle measurements were conducted using a homebuilt setup. The contact angle of the ZrO_2/ODPA layer with water was ~103°. The electrical characteristics of the transistors were measured using HP4156A precision semiconductor parameter analyzers (Agilent Technologies).

III. Results and Discussion
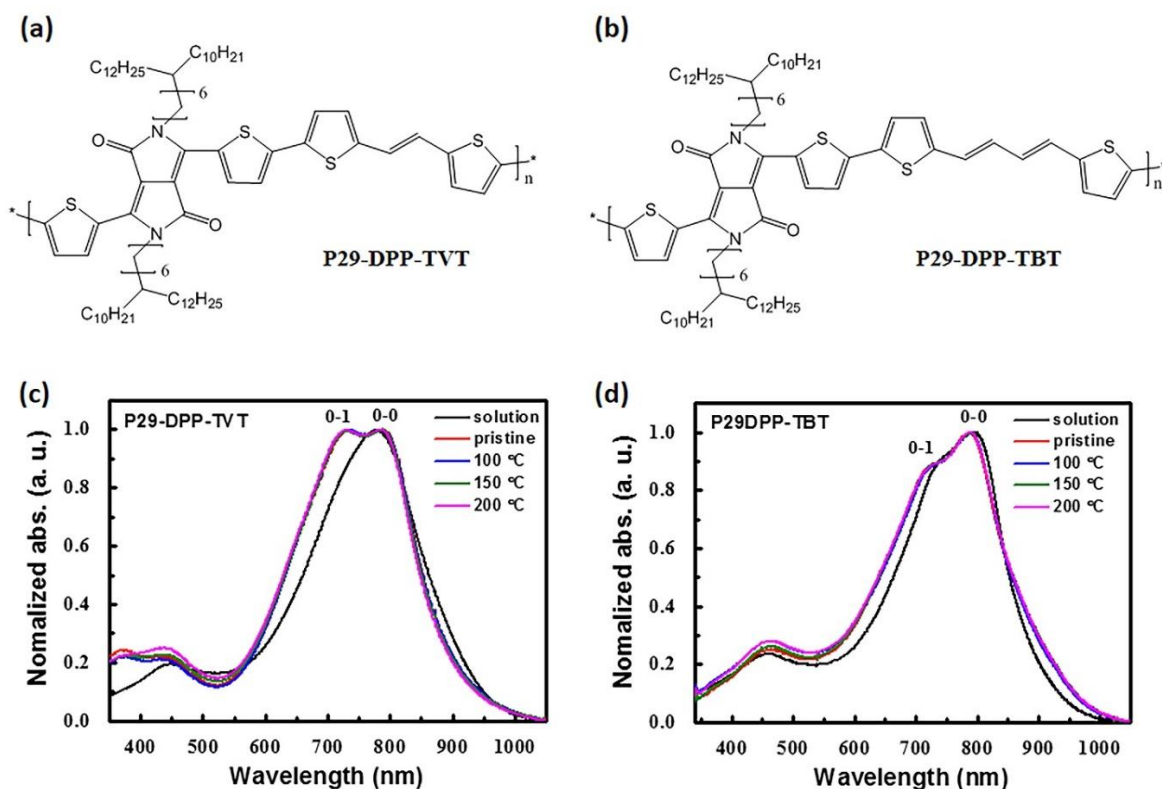
Figure 1.1 Chemical structure of DPP-based donor-acceptor copolymers: (a) reference polymer, P29-DPP-TVT and (b) vinylene-substituted polymer, P29-DPP-TBT. UV-vis absorption spectra: (c) P29-DPP-TVT and (d) P29-DPP-TBT. The solvent of all polymer solutions was chloroform.

The polymer was synthesized via Stille coupling under a nitrogen atmosphere. In a Schlenk flask, 29-DPP-Br (0.20 g, 0.1572 mmol) was added to compound (4) (0.0856 g, 0.1572 mmol) and chlorobenzene (8 mL). After degassing under nitrogen for 30 min, Pd2(dba)3 (2.88 mg, 0.0031 mmol) and P(o-tol)3 (2.87 mg, 0.0094 mmol) were added to the mixture, which was then stirred for 7 days at 90 °C. 2-Bromothiophene and tribu-tyl(thiophene-2-yl)stannane were injected sequentially into the reaction mixture for end-capping, with the solution stirred for 6 h after each addition. After cooling to room temperature, the polymer was precipitated in 150 mL of methanol, and the precipitated solid was collected by filtration and purified by Soxhlet extraction with methanol, acetone, hexane, tetrahydrofuran, and chloroform. The final product, P29-DPP-TBT, was obtained by precipitation in methanol. (Mn = 192 KDa, Mw = 257 KDa , polydispersity index = 1.33, yield: 37.3%) The comparative polymer, P29-DPP-TVT (Mn = 139 KDa, polydispersity index = 1.16), was synthesized as previously reported.[12] The chemical structures of the polymers are shown in Figure 1.1 (a) and (b). P29-DPP-TBT was slightly less soluble compared to P29-DPP-TVT, presumably due to more rigid backbone structure. While P29-DPP-TVT showed very good solubility in chloroform up to 10 mg/ml, P29-DPP-TBT showed limited solubility in chloroform with reasonably transparent solution only up to 7 mg/ml.

To predict the possible structural differences between P29-DPP-TVT and P29-DPP-TBT, DFT calculations were performed using the B3LYP functional and a 6-31G* basis set. Interestingly, substituting butadiene for vinylene reduced the twist angle between the donor and acceptor unit, presumably due to decreased torsional stress. Therefore, extension of the polymer backbone was clearly predicted, which would lead to increased delocalization of both the highest occupied molecular orbital (HOMO) and lowest unoccupied molecular orbital (LUMO). As calculated from the CV curves, the HOMO level of P29-DPP-TVT at −5.41 eV was deeper than that of P29-DPP-TBT at −5.32 eV, implying that P29-DPP-TBT has a more planar backbone structure.

The UV-vis absorption spectra of both polymers were analyzed to determine the distribution of crystalline aggregates. As can be seen from the absorption spectra in Figure 1.1 (c) and (d), both polymers display distinct 0-0 and 0-1 vibronic features, reflecting transitions from the ground state to the first excited state. One distinct difference between the two polymers is that P29-DPP-TBT showed similar absorption features in solution and solid state, but P29-DPP-TVT showed a much more pronounced 0-1 feature in the solid state than in solution. Such an increase in the intensity of the 0-1 peak relative to that of the 0-0 peak on going from solution to the solid state is known to be related to rearrangement of the polymer conformation. Therefore, P29-DPP-TBT has a high level of crystalline aggregation even in solution state, which is not the case for P29-DPP-TVT. The 0-0 and 0-1 peak absorbance ratios in the absorption spectra of P29-DPP-TVT and P29-DPP-TBT are greater than

$$R_{abs} = \frac{A_{0-0}}{A_{0-1}}$$

unity (> 1), which indicates that the J-aggregates model is suitable for calculating the free exciton bandwidth (W) of the polymers:[23-28]

$$R_{abs} = \frac{(1-0.96J_0/w_0)^2}{(1+0.292J_0/w_0)^2}, \quad W = 4|J_0|$$

(1)

where R_{abs} is the ratio of the oscillator strength between 0-0 and 0-1 peak absorbance, J_0 is the nearest neighboring coupling, w_0 is the frequency of nuclear potentials equivalent to shifted harmonic wells.[26]

This equation is valid for the weak coupling regime ($W \ll w_0$) of the J-aggregation model, which is satisfied in our system as shown below. For the calculation of W in our system, we assumed that the C=C symmetric stretch dominated the electron transition, and therefore W could be calculated by setting the w_0 value to 0.18 eV (1450 cm^{-1}).[26, 30] The value of w_0 can be found from Raman spectra analysis conducted by the previous reference which assumed that C=C symmetric stretch from whole conjugated backbone contributed to w_0 value.[30] W is an important parameter for describing conjugation length. The calculated W values imply that the conjugation length in the P29-DPP-TBT film (W = 41.58 meV) was greater than that of the P29-DPP-TVT film (W = 14.84 meV). This observation is consistent with the expectation of DFT calculations, which indicate that extended polymer backbone of P29-DPP-TBT enabled longer conjugation length in solid state.
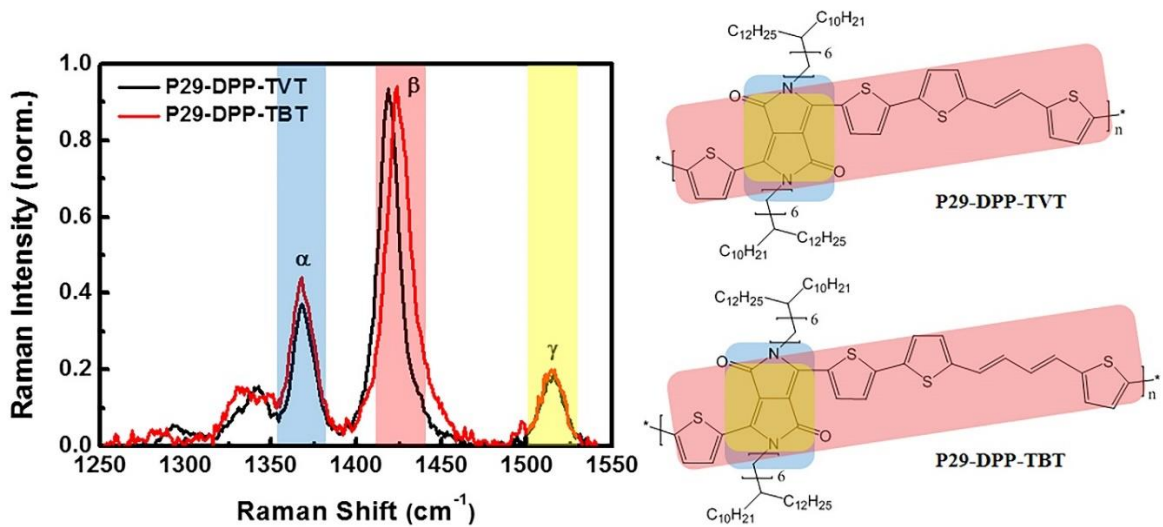
Figure 1.2 Raman spectra for P29-DPP-TVT film and P29-DPP-TBT film. The colored areas of the Raman spectra on the left represent the colored areas of the chemical structure on the right. All polymer films were annealed at 200 °C for 20 min.

We also analyzed the Raman spectra to examine the effect of enhanced backbone planarity on the actual conjugation length. Wood and coworkers reported the Raman spectra peak assignments of DPP-based polymers by DFT geometry optimization results.[29-31] We collected Raman spectra in the range of 1250-1550 cm^{-1}, where peaks corresponding to carbon single bond and carbon double bond stretching are predominant. In Figure 1.2, there are three major peaks observed: α peaks correspond to C–C and C–N symmetric stretches of the DPP acceptor (blue region), β peaks correspond to C–C symmetric stretches of the DPP acceptor and polymer backbone (red region), and γ peaks correspond to C=C symmetric stretches of the DPP acceptor (yellow region). In previous studies, the increases of C–C symmetric stretch peaks relative to C=C symmetric stretch peaks indicate an increase in π electron density, an increase in conjugation length, and an increase in backbone planarity.[29] Unfortunately, in the Raman spectra analysis using excitation with a diode laser at 785 nm, the C=C peak of the polymer backbone was difficult to distinguish because of its relatively low intensity in both polymers. However, the α peaks of P29-DPP-TBT, which are related to backbone planarity, exhibited an increase of 16.4% in peak intensity compared with those of P29-DPP-TVT. Furthermore, β peaks of the P29-DPP-TBT, which are related to the C–C symmetric stretch of DPP acceptor and polymer backbone, were shifted to higher wavenumbers by 5.23 cm^{-1} compared with those of P29-DPP-TVT. In general, a shift to higher wavenumbers for the C–C peaks and a shift to lower wavenumbers for the C=C peaks indicate that the conjugation length has increased, similar to the free exciton bandwidth analyses from UV-vis absorption spectra.[30] The full width at half maximum of the C–C symmetric stretch peaks of P29-DPP-TBT and P29-DPP-TVT were similar at ~15.0 cm^{-1}.
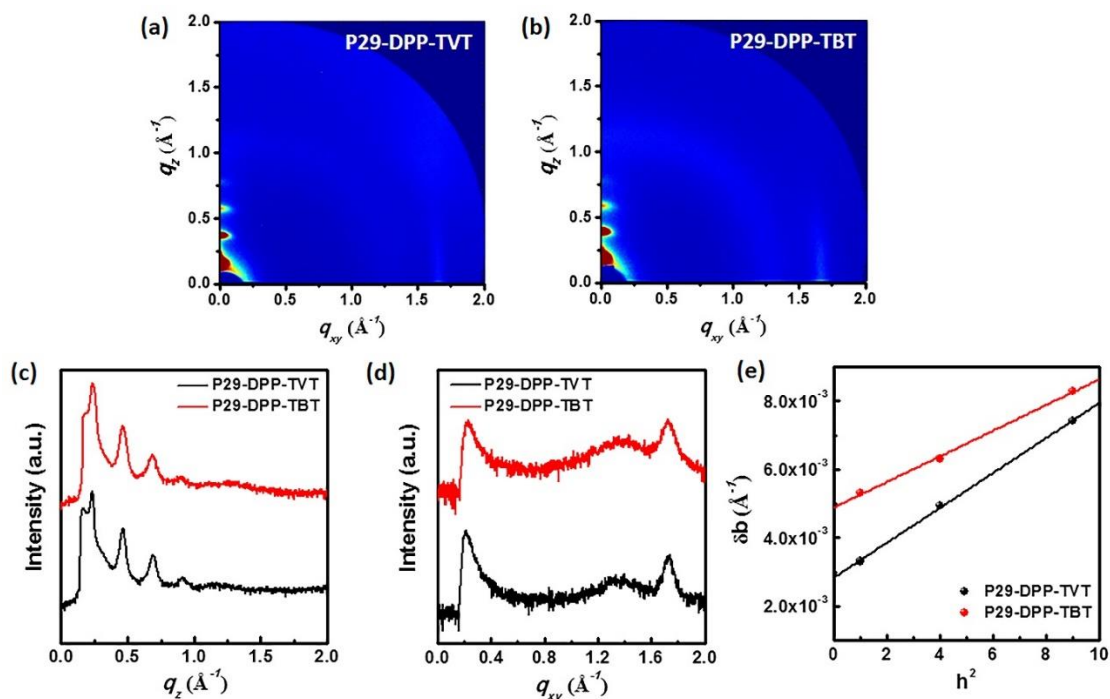
Figure 1.3 2-D-GIXD images measured from (a) P29-DPP-TVT film and (b) P29-DPP-TBT film and their corresponding extracted profiles along with (c) out-of-plane direction and (d) in-plane direction. (e) δb–h^2 plot extracted from each 2-D GIXD profiles. All polymer films were annealed at 200 °C for 20 min.

2-D GIXD and NEXAFS measurements were conducted to study the crystalline characteristics of both polymer films in more detail, which would allow to find the relation between the increased conjugation length and crystalline perfectness. As shown in Figure 1.3, both polymers possess pronounced edge-on orientations, with well-developed Bragg diffraction peaks up to (004) along the q_z direction. From the (010) peak in the q_{xy} direction, which represents the π–π interactions, π–π stacking distances of 3.62 Å were calculated for both polymers. Qualitatively, both polymers exhibited well-developed edge-on orientation and showed small difference.[32] The surface topography images of both polymers measured by AFM were also very similar with R_q values ~1.76 nm, confirming the similar surface morphologies of the two polymers.

While this crystallographic analysis showed that the overall crystalline packing of the polymers was quite similar, the degree of crystalline perfectness required further quantitative analysis. The paracrystalline disorder ($g_{(100)}$) along with q_z direction of organic semiconductors can be calculated from the slope of a δb–h^2 plot (Figure 1.3 (f)) extracted from 2-D GIXD data, where the slope (m) of the δb–h^2 plot is determined by:

$$m = \frac{{g_{(100)}}^2 \cdot \pi^2}{d}$$

$$(2)$$

Where d is the domain spacing, δb is the integral widths of the diffraction peaks, and h is the order of diffraction. To calculate the paracrystalline disorder in the q_{xy} direction, we used a single peak-width estimation using (010) peak.

$$g_{(010)} = \sqrt{\frac{\Delta q}{2\pi q_0}}$$

(3)

Where $g_{(010)}$ is the paracrystalline disorder in the q_{xy} direction, Δq is the breadth of a diffraction peak, and q_0 is the center position of peak.[33]

Interestingly, P29-DPP-TBT with increased conjugation length had a lower level of paracrystalline disorder ($g_{(010)} = 8.05$, $g_{(100)} = 3.17$) than P29-DPP-TVT ($g_{(010)} = 8.47$, $g_{(100)} = 3.71$) in both the q_z and q_{xy} directions.
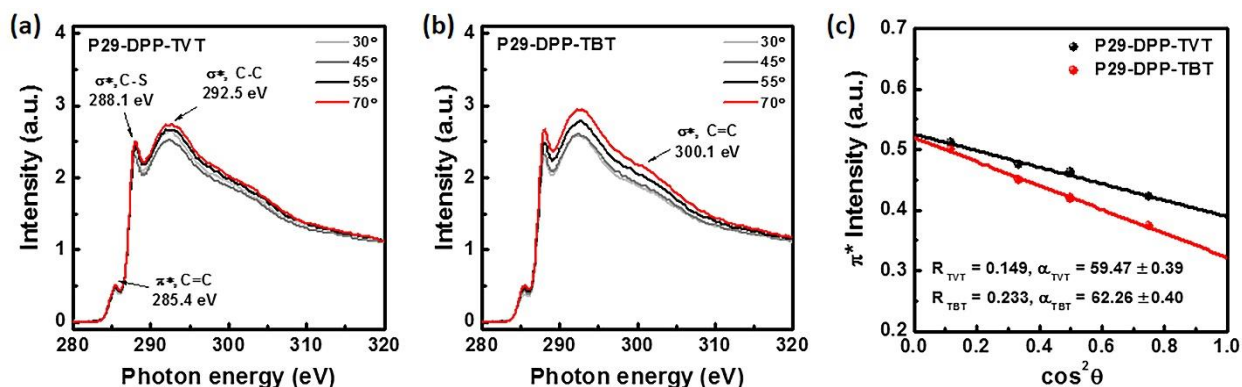
Figure 1.4 Carbon K-edge NEXAFS spectra for (a) P29-DPP-TVT film and (b) P29-DPP-TBT film, and (c) π* orbital orientation analysis for both polymers. All polymer films were annealed at 200 °C for 20 min.

NEXAFS measurements of the same samples, enabled us to obtain more detailed surface crystalline orientation information than 2-D GIXD measurements. We obtained the average tilting angle of the polymer backbone against the substrate by analyzing NEXAFS spectra measured at various incident X-ray angles. The NEXAFS spectra of both polymers are summarized in Figure 1.4. By plotting the π* resonance (285.4 eV) as a function of $\cos^2\theta$, where θ is the incident angle, we obtained the dichroic ratio (R) as well as the average tilting angle (α) of the polymer backbone. As summarized in Figure 1.4 (c), the α of P29-DPP-TVT was ~59.47 ± 0.39 ° ($R = 0.149$), whereas that of P29-DPP-TBT was ~62.26 ± 0.40 ° ($R = 0.233$).[34, 35] Collectively, the crystalline perfectness analysis of 2-D GIXD and crystalline orientation analysis of NEXAFS suggested that the thin film of P29-DPP-TBT possessed lower paracrystalline disorder and a less tilted backbone orientation compared with

that of P29-DPP-TVT. Considering the DFT calculations and free exciton bandwidth predictions as well as Raman analyses, we can argue that substituting a butadiene linkage or a vinylene linkage resulted in a more planar polymer backbone, which in turn facilitated more efficient intermolecular interactions, finally leading to more perfect crystalline structure.
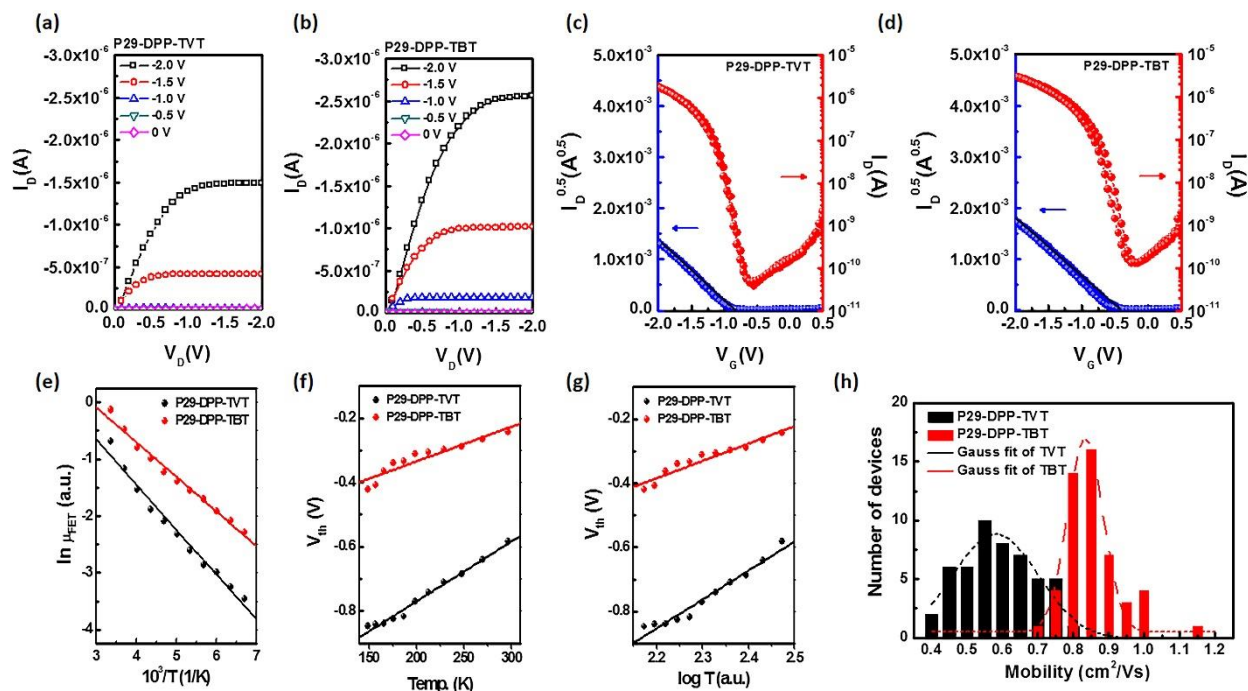
Figure 1.5. The representative transfer curves and output characteristics of (a,c) P29-DPP-TVT-based PFET and (b,d) P29-DPP-TBT-based PFET. (e) Temperature dependence of charge carrier mobilities and (f) V_{th}. (g) Logarithmic temperature dependence of V_{th}. (h) Device-to-device deviation of charge carrier mobility comparison in P29-DPP-TVT-based PFETs and P29-DPP-TBT-based PFETs. All PFETs were annealed at 200 °C for 20 min.

We fabricated bottom-gate/top-contact FETs of P29-DPP-TVT and P29-DPP-TBT using ZrO_2/ODPA-treated Si (n^{+2}) as the dielectric/substrate layer. For low-voltage operation, we used ZrO_2 with a high dielectric constant as an insulating layer and improved the performance by using the ODPA layer as a self-assembled monolayer. The representative transfer and output characteristics are shown in Figure 1.5, and all the FET parameters are listed in Table 1.1. Without encapsulation, FETs of both polymers showed pretty good air stability with nearly identical transfer characteristics against ambient exposure up to seven days. The highest charge carrier mobility was calculated to be 0.76 cm² V⁻¹ s⁻¹ for P29-DPP-TVT and 1.15 cm² V⁻¹ s⁻¹ for P29-DPP-TBT. To conduct a more detailed comparative study of the charge transport nature of the polymers, we analyzed the tem-

perature dependence of their charge transfer characteristics. In a plot of $I_{DS}^{0.5}$ vs. V_{GS} measured in the off-to-on sweep direction (Figure 1.5 (c) and (d)), the mobility of the device decreased as the measurement temperature decreased. The positive relationship between temperature and mobility clearly indicates that a hopping transport mechanism is valid in both polymers, which is consistent with other high mobility polymer semiconductors.[36] The obtained mobilities are plotted as a function of inverse temperature in Figure 1.5 (e), and the results demonstrate that the temperature dependence of the charge carrier mobility follows Arrhenius behavior. The Arrhenius activation energies were estimated to be ~68.08 and 52.39 meV for P29-DPP-TVT and P29-DPP-TBT, respectively, which are comparable or slightly lower compared to other reports.[37-39] The threshold voltage (V_{th}) shift was also monitored as a function of temperature, as summarized in Figure 1.5 (f). Using the equation:[40]

$N_{tr} = \frac{C_i V_{th}}{e}$, we can approximate the concentration of deep trap states to be ~ 1.26×10^{12} and 5.24×10^{11} cm^{-2} for P29-DPP-TVT and P29-DPP-TBT, respectively, at room temperature. As the temperature decreases, the density of deep trap states increases up to 1.85×10^{12} and 9.20×10^{11} cm^{-2} for P29-DPP-TVT and P29-DPP-TBT, respectively, at 149 K. Considering that, the charge carrier hopping rate between sites i and j in the hopping transport model can be expressed by $v_{ij} \sim exp\left(-\frac{E_j - E_i}{kT}\right)$,[41] the increased trap densities at low temperatures also strongly support the presence of a hopping transport model in these two polymers. Furthermore, the

logarithmic temperature dependence of V_{th} (Figure 1.5 (g)) and the relationship $\frac{\partial N_{tr}}{\delta E} \sim \frac{\partial V}{\partial T}$ [40] suggest that the trap distribution in our polymers above their HOMO levels follow an exponential distribution, which is similar to that of amorphous Si.[40] These results clearly explain the lower trap density of P29-DPP-TBT compared with that of P29-DPP-TVT and are in good agreement with the previous observation of a lower paracrystalline disorder and more planar backbone for P29-DPP-TBT.

Table 1.1 PFETs electrical characteristics

Polymer	μ (cm² V⁻¹ s⁻¹)		V_{th} (V)	$I_{D,max.}$ (μA)	I_{on} / I_{off}	E_a (meV)	N_{tr} (cm⁻²)
	Max.	Ave.[a]					
P29-DPP-TVT	0.76	0.58±0.10	-0.61±0.13	1.59	10^5	68.08±3.18	1.26×10^{12}
P29-DPP-TBT	1.15	0.86±0.08	-0.42±0.10	3.08	10^5	52.39±2.17	5.24×10^{11}

[a]Mobility values were summarized from 50 devices for each polymer based FETs. All PFETs were annealed at 200 °C for 20 min.

In addition to the higher charge carrier mobility, the FET performances reliabilty was also enhanced by substituting butadiene for vinylene in the donor building block. To investigate the reliability of FET devices, we fabricated 50 independent FET devices for each polymer and determined their statistical performance characteristics, as summarized in Figure 1.5 (h). The Gaussian fit of the statistical data clearly showed that P29-DPP-TBT yielded more reliable and reproducible FET performance compared with that of P29-DPP-TVT. We believe that the lower trap density of P29-DPP-TBT enabled this good reliability.

IV. Conclusion

The effects of the conjugation structure of the donor moiety on the crystalline features and charge transport characteristics of donor-acceptor copolymers were systematically investigated based on a comparison of newly synthesized P29-DPP-TBT with P29-DPP-TVT. P29-DPP-TBT, with butadiene linkages between thiophene units, was strategically designed to extend the polymer backbone planarity as predicted by DFT calculations. Free exciton bandwidth calculations from UV-vis absorption spectra and Raman spectra analyses showed that P29-DPP-TBT have a more extended polymer backbone with an increased effective conjugation length, when compared with P29-DPP-TVT. In-depth X-ray analysis showed that the crystalline perfectness of P29-DPP-TBT was superior that of P29-DPP-TVT which can be attributed to above mentioned enhanced conjugation length. This result was further confirmed by temperature-dependent FET analysis, which showed

lower trap densities in FETs based on P29-DPP-TBT compared with those based on P29-DPP-TVT. The resulting charge carrier mobility of 1.15 cm^2 V^{-1} s^{-1} in P29-DPP-TBT was 50% higher than that in P29-DPP-TVT. Moreover, the reproducibility of the high FET performance was also more reliable in the case of P29-DPP-TBT. We argue that optimizing the donor conjugation structure by increasing the conjugation length can dramatically change the backbone planarity and crystalline characteristics of the final polymer film, and thus the charge transport nature of the device. We believe that the results of this study will be an indicator of the molecular design for improving the charge transport of new class high-performance donor-acceptor copolymers such as DPP, IID, NDI, and BBT, which have been actively studied recently.

V. References

[1]   Klauk, H. *Organic Electronics II: More Materials and Applications*; Wiley-VCH: Weinheim, 2012.

[2]   Yadav, S. and Ghosh, S., 2016. Amorphous strontium titanate film as gate dielectric for higher performance and low voltage operation of transparent and flexible organic field effect transistor. ACS applied materials & interfaces, 8(16), pp.10436-10442.

[3]   Lee, M.Y., Hong, J., Lee, E.K., Yu, H., Kim, H., Lee, J.U., Lee, W. and Oh, J.H., 2016. Highly flexible organic nanofiber phototransistors fabricated on a textile composite for wearable photosensors. Advanced Functional Materials, 26(9), pp.1445-1453.

[4]   Ren, X., Pei, K., Peng, B., Zhang, Z., Wang, Z., Wang, X. and Chan, P.K., 2016. A low-operating-power and flexible active-matrix organic-transistor temperature-sensor array. Advanced Materials, 28(24), pp.4832-4838.

[5]   Steudel, S., Myny, K., Schols, S., Vicca, P., Smout, S., Tripathi, A., Van Der Putten, B., van der Steen, J.L., Van Neer, M., Schütze, F. and Hild, O.R., 2012. Design and realization of a flexible QQVGA AMOLED display with organic TFTs. Organic Electronics, 13(9), pp.1729-1735.

[6]   Sirringhaus, H., Brown, P.J., Friend, R.H., Nielsen, M.M., Bechgaard, K., Langeveld-Voss, B.M.W., Spiering, A.J.H., Janssen, R.A., Meijer, E.W., Herwig, P. and De Leeuw, D.M., 1999. Two-dimensional charge transport in self-organized, high-mobility conjugated polymers. Nature, 401(6754), pp.685-688.

[7]   McCulloch, I., Heeney, M., Bailey, C., Genevicius, K., MacDonald, I., Shkunov, M., Sparrowe, D., Tierney, S., Wagner, R., Zhang, W. and Chabinyc, M.L., 2006. Liquid-crystalline semiconducting polymers with high charge-carrier mobility. Nature materials, 5(4), pp.328-333.

[8]   Li, Y., Sonar, P., Singh, S.P., Soh, M.S., van Meurs, M. and Tan, J., 2011. Annealing-Free High-Mobility Diketopyrrolopyrrole− Quaterthiophene Copolymer for Solution-Processed Organic Thin Film Transistors. Journal of the American Chemical Society, 133(7), pp.2198-2204.

[9]   Zhang, W., Smith, J., Watkins, S.E., Gysel, R., McGehee, M., Salleo, A., Kirkpatrick, J., Ashraf, S., Anthopoulos, T., Heeney, M. and McCulloch, I., 2010. Indacenodithiophene semiconducting polymers for high-performance, air-stable transistors. Journal of the American Chemical Society, 132(33), pp.11437-11439.

[10]   Cho, J., Park, S.J., Lee, S.M., Ha, J.U., Ahn, E.S., Chang, S.T., Kwon, S.K., Chung, D.S. and Kim, Y.H., 2016. Synergetic Evolution of Diketopyrrolopyrrole-Based Polymeric Semiconductor for High Reproducibility and Performance: Random Copolymerization of Similarly Shaped Building Blocks. Macromolecular rapid communications, 37(24), pp.2057-2063.

[11]   Ding, L., Li, H.B., Lei, T., Ying, H.Z., Wang, R.B., Zhou, Y., Su, Z.M. and Pei, J., 2012. Alkylene-chain effect on microwire growth and crystal packing of π-moieties. Chemistry of Materials, 24(10), pp.1944-1949.

[12]   Kang, I.L., Yun, H.J., Chung, D.S., Kwon, S.K. and Kim, Y.H., 2013. Record high hole mobility in polymer semiconductors via side-chain engineering. Journal of the American Chemical Society, 135(40), pp.14896-14899.

[13]   Han, A.R., Dutta, G.K., Lee, J., Lee, H.R., Lee, S.M., Ahn, H., Shin, T.J., Oh, J.H. and Yang, C., 2015. ε-Branched flexible side chain substituted diketopyrrolopyrrole-containing polymers designed for high hole and electron mobilities. Advanced Functional Materials, 25(2), pp.247-254.

[14]   Lei, T., Cao, Y., Fan, Y., Liu, C.J., Yuan, S.C. and Pei, J., 2011. High-performance air-stable organic field-effect transistors: isoindigo-based conjugated polymers. Journal of the American Chemical Society, 133(16), pp.6099-6101.

[15]   Yan, H., Chen, Z., Zheng, Y., Newman, C., Quinn, J.R., Dötz, F., Kastler, M. and Facchetti, A., 2009. A high-mobility electron-transporting polymer for printed transistors. Nature, 457(7230), pp.679-686.

[16]   Fan, J., Yuen, J.D., Cui, W., Seifter, J., Mohebbi, A.R., Wang, M., Zhou, H., Heeger, A. and Wudl, F., 2012. High-Hole-Mobility Field-Effect Transistors Based on Co-Benzobisthiadiazole-Quaterthiophene. Advanced Materials, 24(46), pp.6164-6168.

[17]   Noriega, R., Rivnay, J., Vandewal, K., Koch, F.P., Stingelin, N., Smith, P., Toney, M.F. and Salleo, A., 2013. A general relationship between disorder, aggregation and charge transport in conjugated polymers. Nature materials, 12(11), pp.1038-1044.

[18]   Himmelberger, S., Vandewal, K., Fei, Z., Heeney, M. and Salleo, A., 2014. Role of molecular weight distribution on charge transport in semiconducting polymers. Macromolecules, 47(20), pp.7151-7157.

[19]   Yu, H., Park, K.H., Song, I., Kim, M.J., Kim, Y.H. and Oh, J.H., 2015. Effect of the alkyl spacer length on the electrical performance of diketopyrrolopyrrole-thiophene vinylene thiophene polymer semiconductors. Journal of Materials Chemistry C, 3(44), pp.11697-11704.

[20]   McCulloch, I., Salleo, A. and Chabinyc, M., 2016. Avoid the kinks when measuring mobility. Science, 352(6293), pp.1521-1522.

[21]   Park, Y.M., Desai, A., Salleo, A. and Jimison, L., 2013. Solution-processable zirconium oxide gate dielectrics for flexible organic field effect transistors operated at low voltages. Chemistry of Materials, 25(13), pp.2571-2579.

[22]   Park, Y.M., Daniel, J., Heeney, M. and Salleo, A., 2011. Room-temperature fabrication of ultrathin oxide gate dielectrics for low-voltage operation of organic field-effect transistors. Advanced Materials, 23(8), pp.971-974.

[23]   Yamagata, H., Hestand, N.J., Spano, F.C., Köhler, A., Scharsich, C., Hoffmann, S.T. and Bässler, H., 2013. The red-phase of poly [2-methoxy-5-(2-ethylhexyloxy)-1, 4-phenylenevinylene](MEH-PPV): A disordered HJ-aggregate. The Journal of chemical physics, 139(11), p.114903.

[24]   Spano, F.C. and Silva, C., 2014. H-and J-aggregate behavior in polymeric semiconductors. Annual review of physical chemistry, 65, pp.477-500.

[25]   Spano, F.C., 2010. The spectral signatures of Frenkel polarons in H-and J-aggregates. Accounts of chemical research, 43(3), pp.429-439.

[26]   Kobayashi, T., 2012. J-aggregates (Vol. 2). World Scientific.

[27]   Spano, F.C., 2005. Modeling disorder in polymer aggregates: The optical spectroscopy of regioregular poly (3-hexylthiophene) thin films. The Journal of chemical physics, 122(23), p.234701.

[28]   Clark, J., Chang, J.F., Spano, F.C., Friend, R.H. and Silva, C., 2009. Determining exciton bandwidth and film microstructure in polythiophene films using linear absorption spectroscopy. Applied Physics Letters, 94(16), p.117.

[29]   Fei, Z., Boufflet, P., Wood, S., Wade, J., Moriarty, J., Gann, E., Ratcliff, E.L., McNeill, C.R., Sirringhaus, H., Kim, J.S. and Heeney, M., 2015. Influence of Backbone Fluorination in Regioregular Poly (3-alkyl-4-fluoro) thiophenes. Journal of the American Chemical Society, 137(21), pp.6866-6879.

[30]   Wood, S., Wade, J., Shahid, M., Collado-Fregoso, E., Bradley, D.D., Durrant, J.R., Heeney, M. and Kim, J.S., 2015. Natures of optical absorption transitions and excitation energy dependent photostability of diketopyrrolopyrrole (DPP)-based photovoltaic copolymers. Energy & Environmental Science, 8(11), pp.3222-3232.

[31]   Tsoi, W.C., James, D.T., Kim, J.S., Nicholson, P.G., Murphy, C.E., Bradley, D.D., Nelson, J. and Kim, J.S., 2011. The nature of in-plane skeleton Raman modes of P3HT and their correlation to the degree of molecular order in P3HT: PCBM blend thin films. Journal of the American Chemical Society, 133(25), pp.9834-9843.

[32]   Rivnay, J., Mannsfeld, S.C., Miller, C.E., Salleo, A. and Toney, M.F., 2012. Quantitative determination of organic semiconductor microstructure from the molecular to device scale. Chemical reviews, 112(10), pp.5488-5519.

[33]   Rivnay, J., Noriega, R., Kline, R.J., Salleo, A. and Toney, M.F., 2011. Quantitative analysis of lattice disorder and crystallite size in organic semiconductor thin films. Physical Review B, 84(4), p.045203.

[34]   Salleo, A., Kline, R.J., DeLongchamp, D.M. and Chabinyc, M.L., 2010. Microstructural characterization and charge transport in thin films of conjugated polymers. Advanced Materials, 22(34), pp.3812-3838.

[35]   Jang, M., Kim, S.H., Lee, H.K., Kim, Y.H. and Yang, H., 2015. Layer-by-Layer Conjugated Extension of a Semiconducting Polymer for High-Performance Organic Field-Effect Transistor. Advanced Functional Materials, 25(25), pp.3833-3839.

[36]   Coropceanu, V., Cornil, J., da Silva Filho, D.A., Olivier, Y., Silbey, R. and Brédas, J.L., 2007. Charge transport in organic semiconductors. Chemical reviews, 107(4), pp.926-952.

[37]   Ha, T.J., Sonar, P. and Dodabalapur, A., 2013. Charge transport study of high mobility polymer thin-film transistors based on thiophene substituted diketopyrrolopyrrole copolymers. Physical chemistry chemical physics, 15(24), pp.9735-9741.

[38]   Gruber, M., Jung, S.H., Schott, S., Venkateshvaran, D., Kronemeijer, A.J., Andreasen, J.W., McNeill,

C.R., Wong, W.W., Shahid, M., Heeney, M. and Lee, J.K., 2015. Enabling high-mobility, ambipolar charge-transport in a DPP-benzotriazole copolymer by side-chain engineering. Chemical science, 6(12), pp.6949-6960.

[39]   Kronemeijer, A.J., Gili, E., Shahid, M., Rivnay, J., Salleo, A., Heeney, M. and Sirringhaus, H., 2012. A selenophene-based low-bandgap donor–acceptor polymer leading to fast ambipolar logic. Advanced Materials, 24(12), pp.1558-1565.

[40]   Podzorov, V., Menard, E., Borissov, A., Kiryukhin, V., Rogers, J.A. and Gershenson, M.E., 2004. Intrinsic charge transport on the surface of organic semiconductors. Physical review letters, 93(8), p.086602.

[41]   Bässler, H., 1993. Charge transport in disordered organic photoconductors a Monte Carlo simulation study. physica status solidi (b), 175(1), pp.15-56.

Part 2. Facilitating Phase Transfer of Polymer Semiconductor in Mini-Emulsion Synthesis via Molecular Affinity Engineering

I. Introduction

In recent decades, polymer semiconductors with low cost, flexibility and solution processability have been regarded as promising candidates as the active layer of next generation electronic devices. Therefore, intensive research efforts have been conducted and as a result, the charge carrier mobility of polymer semiconductors has been improved to the point that it has exceeded that of amorphous silicon semiconductors.[1-4] Nonetheless, their solution processability, which is the most important advantage provided by their use, is actually based on toxic organic solvents which is strictly limited by government regulations. As a solution to this issue, water-borne polymer semiconductors provided by mini-emulsion synthesis are considered environmentally friendly candidates.[5-8] Mini-emulsion synthesis, in which two immiscible liquid phases are mixed using a surfactant, can produce uniform polymer colloids (nanoparticles of less than 100 nm) dispersed in water. Since Landfester et al. first introduced mini-emulsion synthesis of polymer semiconductors by using sodium dodecylsulfate (SDS), many researchers have reported relatively low but meaningful opto-electronic performances from water-borne polymer semiconductors.[5-9] More recently, researchers started to consider other surfactants other than only SDS, to expand the feasibility of mini-emulsion synthesis of polymer semiconductors and to enhance semiconductor properties.[10-12] Chung et al. showed that a surfactant molecule which optimizes emulsification efficiency can lead to successful mini-emulsion synthesis, by decreasing colloid size and thus leading to fine film quality.[11] Another research trends in this field is developing processing methods to remove surfactants after thin film fabrication procedure. Up to now, it has been reported that the removal of surfactants by dialysis, pyrolysis, and post-solvent treatment can improve the performance of opto-electronic devices.[7-9] Unfortunately, however, there have been no research efforts to optimize molecular structure of polymer semiconductor itself so that overall quality of water-borne polymer semiconductors can be improved.

In the early stages of mini-emulsion study, research efforts were directed towards the traditional donor-type, mono-polar, helix-structured polythiophene, which can be produced relatively easily as a stable water-borne colloid.[5, 6] However, recently reported high performance polymer semiconductors, such as diketopyrrolopyrrole (DPP), isoindigo, thieno[3,4-c]pyrrole-4,6-dione, bithiophenesulfonamide, and naphthalene diimide derivatives, are much easier to aggregate than conventional polymer semiconductors even in good solvents, because of their planar backbone molecular structures.[13-17] This, in turn, makes it more difficult for mini-emulsion synthesis to produce stable water-borne colloids because mini-emulsion is basically about phase trans-

fer of hydrophobic polymers from organic phase to water phase. Therefore, when a mini-emulsion synthesis is carried out with polymer semiconductors that have planar backbone structures, suitable chemical modification should be introduced so that successful mini-emulsion synthesis can be achieved in combination with pre-developed surfactant optimization.

In order to synthesize a polymer semiconductor suitable for mini-emulsion synthesis, we focused on these issues: 1) how to synthesize small-sized colloidal particles which can be delivered by enhancing emulsification efficiency and 2) how to maintain such small-sized particles until the final stage of solidification process which can be achieved by minimizing depletion contact energy of colloidal solution. Both the aforementioned factors are extremely important to realize efficient coalescence which in turn leads to high quality thin films of polymer semiconductors, because the degree of coalescence between the colloid particles during the solidification that produces continuous thin film is inversely proportional to the particle size.

To this end, we designed a new DPP-based donor-acceptor polymer semiconductors whose functionalized alkyl side chains can facilitate highly efficient mini-emulsion synthesis. Diketopyrrolopyrrole-thiophene-vinylene-thiophene (DPP-TVT), which is a representative high performance, planar polymer semiconductor, was selected as a reference polymer semiconductor, and its Si-analogue, SiDPP-TVT, in which the carbon atoms of the branched alkyl chains of DPP-TVT were replaced with silicon atoms, is newly synthesized. By substituting silicon at the branching position of the alkyl side chain, the volumetric portion of the alkyl side chain is expanded by increasing the C-Si-C bond angle and the Si-C bond length compared to the conventional C-C-C bond angle and C-C bond length.[18, 19] The extension of the alkyl side chain group could increase the solubility and hydrophobicity of the synthesized SiDPP-TVT, which enables better molecular affinity with ionic surfactant. First, because of the increased solubility of SiDPP-TVT, we can expect that larger surface areas of the individual polymer chains in organic phase will be exposed to the surfactants in water phase during mini-emulsion synthesis. Second, due to the increased hydrophobicity of SiDPP-TVT, we can expect that the van der Waals interaction between the side chain of polymer semiconductor and the tail group of surfactants will be enhanced. These two effects can synergetically facilitates molecular affinity between polymer semiconductor and surfactants, or emulsification efficiency, resulting in smaller particle sizes and their more uniform size distribution. We have succeeded in synthesizing smaller and uniform colloids by using SiDPP-TVT, and have demonstrated more advanced results in terms of not only charge carrier mobility but also reproducibility which was required but not yet filled room for mini-emulsion-based electronic devices. We believe that this systematic study on polymer semiconductor design for efficient mini-emulsion synthesis can advance the era of better

environmentally benign polymer electronics.

II. Experimental Section

2.1 Materials

Pd2(dba)3 and P(o-Tol)3 were purchased from Stream. All reactions were performed under a nitrogen atmosphere using standard Schlenk techniques. In addition, all chemical reagents were purchased from Aldrich and used as received. Detailed polymer synthesis methods and related information can be found in supporting information. The DPP-TVT was synthesized using a previously reported method.[33].

2.2 Colloid synthesis

Solutions consisting of 40 mg/ml of CTAB in water and a sufficiently dissolved 2 mg/ml polymer in chloroform were mixed, heated, and stirred at 70 °C for 2 hours. The chloroform was evaporated completely from the colloidal solution, and then it was checked by passing through a 0.2-µm filter.[11].

2.3 Device fabrication

A bare Si wafer was used as the substrate, and a ZrO_x dielectric layer was prepared via a method commonly used in previous studies: the ZrO_x sol-gel method.[34] The octadecylphosphonic acid (ODPA) self-assembled monolayers were deposited by immersing them to both neatly improve the robustness of the ZrO_x dielectric layer's film and reduce the number of electrical traps.[35] The active layer was coated onto the ZrO_x/ODPA-treated substrate with solutions of either DPP-TVT or SiDPP-TVT in chloroform or mini-emulsion. After the coating with a colloidal solution, the remaining surfactant was removed by soaking it in ethanol for 3 min. To enhance the molecular ordering among the DPP molecules, the prepared films were annealed at various temperatures (between 100−200 °C) for 20 min and then cooled slowly. Finally, the OFET's geometry was completed by depositing Au source-drain electrodes onto the annealed films (with channel width/length ratios of 10−20 and channel lengths of 75−150 µm).

2.4 Characterization

The 2D-GIXD measurements were performed using the PLS-II 3C and 9A beamline at the Pohang Accelerator Laboratory (PAL) in Korea. All films were manufactured in the same manner that the devices were fabricated. In the surface sample analyses, the HR-TEM (Hitachi, HF-3300), AFM (Park Systems, XE-150), SEM (Hitachi, SU8230), and FT-IR measurements (Thermo Scientific, Continuum) were performed carefully after discussion with C. Park, K. Kim and J. Park in the Center for Core Research Facilities of the Daegu Gyeongbuk Institute of Science and Technology.

2.5 Measurements

UV−Vis. absorption spectra were measured using a UV-1650PC spectrophotometer. The capacitance values of the dielectric layers were measured using a Keysight E4981 capacitance meter operating at 1 kHz. The capacitance of the ZrO$_x$/ODPA layer was 3.4×10^{-7} F cm^{-2} at this frequency. The contact-angle measurements were collected using a home-built setup. Finally, the electrical characteristics of the transistors were measured using a parameter analyzer (Keithley, 4200A-SCS). The V$_{DS}$ was -2 V when measuring the transfer curves and output curves.

III. Results and Discussion

2.1. Efficiency of Mini-emulsion

In order to realize high quality thin films from water-borne colloids, coalescence efficiency should be maximized. A coalescence phenomenon occurs by capillary pressure of trapped water between colloid particles, and therefore, the degree of coalescence can be estimated by:

$$P_c \approx \gamma_w / R \tag{1}$$

where Pc is the capillary pressure, γ_w is the air-water interfacial surface tension, and R is the particle radius.[20] Therefore, synthesizing small-sized particles from mini-emulsion synthesis is of primary importance. However, during solidification of the colloidal solution when the solute concentration rapidly increases, there is a strong driving force causing increases of particle size, which is related with depletion contact energy. The following equations can be used to calculate the depletion contact energy of colloids:

$$u_c^s = -(1/4)\pi P \sigma_2 \sigma_1^2 \tag{2}$$

and

$$P = nkT \,,\tag{3}$$

where u_c^ξ is the depletion contact energy of the spherical colloid, P is the overall osmotic pressure, σ_1 is the exclusion diameter of the micelles (which is roughly shorter than 5 nm), σ_2 is the diameter of the synthesized colloid, n is the micelle concentration, k is the Boltzmann constant, and T is the temperature.[21-23] Therefore, one can see that not only the decreasing particle size at the stage of mini-emulsion synthesis, but also suppressing the particle-to-particle size deviation is very important to minimize depletion contact energy. As briefly explained in Figure 2.1a depletion contact energy can be maximized when the particle size is large and its size distribution is also high, leading to significant aggregation in colloids before solidification. In this case, as explained earlier, the coalescence phenomenon is not efficient, resulting in a very rough morphology. In other words, synthesizing colloidal particles with small and narrowly distributed size is most important to render high quality thin films of polymer semiconductor. Now, we need to take into account what properties the polymer semiconductors should have to make such small particles with narrow size distribution through mini-emulsion synthesis.
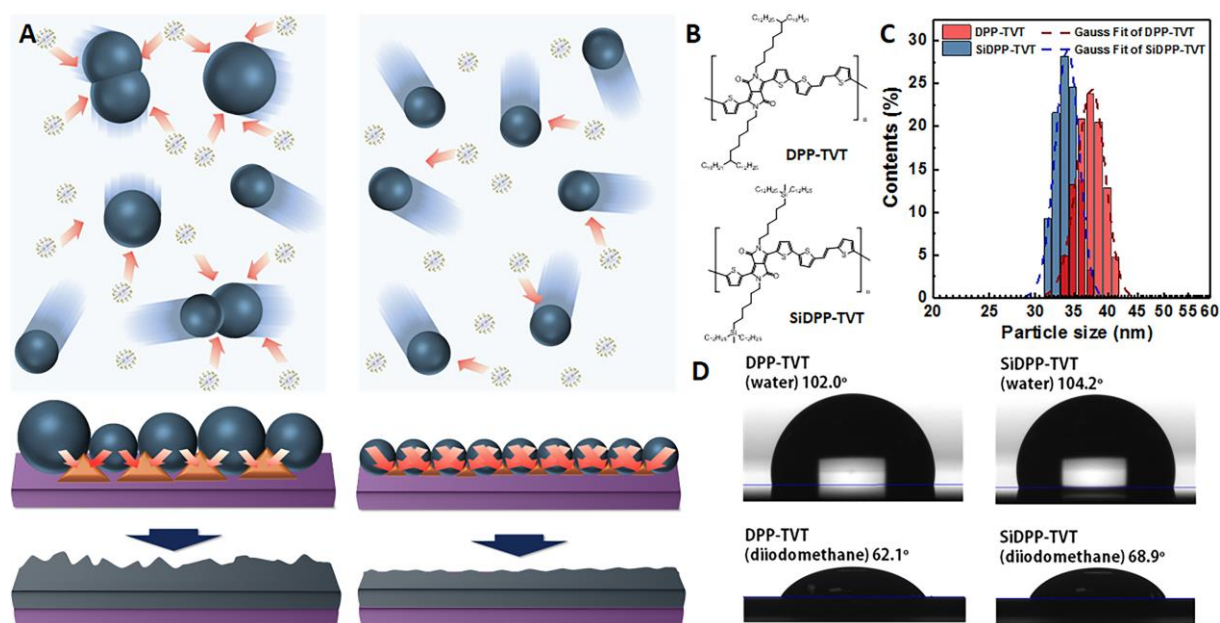
Figure 2.1 (a) The schematic diagram for describing depletion contact energy in solution and coalescence phenomenon by differences of colloid size and distribution. (b) Chemical structure of DPP-TVT and SiDPP-TVT. (c) The DLS measurement results of particle size distribution of DPP-TVT and SiDPP-TVT dissolved in chloroform. (d) The contact angle images of DPP-TVT and SiDPP-TVT with water and diiodomethane to calculate surface energy.

The mini-emulsion synthesis is initiated by mixing a polymer semiconductor dissolved in an organic solvent and a surfactant dissolved in water. Here, the size and uniformity of the colloid of the polymer semiconductor is determined at the phase transfer step where hydrophobic polymer semiconductor is transferred from organic phase to water phase. In this regard, it is important to increase the chance of physical interaction between an individual polymer semiconductor and a surfactant molecule. Therefore, firstly, it is expected that increasing the solubility of polymer semiconductor in the organic phase is critical because polymer semiconductors present in separate chains rather than entangled clusters would increase the likelihood of encountering an individual polymer semiconductor and a surfactant molecule. Secondly, it is expected that strengthening van der Waals interaction between hydrophobic solubilizing groups of the polymer semiconductor and the hydrophobic tail of surfactants can also facilitate the physical interaction between an individual polymer semiconductor and a surfactant molecule. Collectively, we can assume that increasing solubility and hydrophobicity of polymer semiconductor can lead to an improvement in molecular affinity against surfactants, leading to high emulsification efficiency and thus small/uniform particles, which can result in efficient coalescence phenomenon.

From this point of view, we designed and synthesized a new polymer semiconductor with the aim of maintaining the high semiconducting properties even when its film is cast from water-borne colloids, by modifying solubility and hydrophobicity of the conventional high performance polymer semiconductor. We selected a DPP derivative polymer semiconductor, DPP-TVT, represented by high performance p-type field-effect transistor performances but also by relatively worse solubility caused by the planar backbone structure compared to other traditional donor-polymer semiconductors. To improve solubility and hydrophobicity of DPP-TVT, we focused on the atom at branching position of the alkyl solubilizing group, which occupies an important position in determining the total volumetric portion of the alkyl group. In this context, SiDPP-TVT is synthesized by replacing the branching point carbon of the alkyl solubilizing groups by the silicon atom of the reference high performance polymer semiconductor, DPP-TVT, as shown in Figure 2.1b. On the chemical structure side, the Si-C bond length (1.86 Å) is longer than the C-C bond length (1.54 Å). In addition, the C-C-C bond angle of the carbon atoms in the branched alkyl position of the DPP-TVT is 109.5 °, which is enlarged to 114.0 ° in the case of C-Si-C bond angle of SiDPP-TVT.[18, 19] Therefore, as a result of Si-substitution in branching point, one can expect the increase in the volumetric portion of the bulky alkyl group in overall polymer semiconductors, which might lead to enhancement of solubility and hydrophobicity. Actually, as shown in the dynamic light scattering (DLS) measurement in Figure 2.1c, the Z-average value of DPP-TVT dissolved in chloroform is 37.44 nm and that of SiDPP-TVT is 34.08 nm, indicative of increased solubility of SiDPP-TVT in organic phase. In the pre-

sent study, we synthesized both DPP-TVT and SiDPP-TVT with similar molecular weights to avoid solubility changes caused by differing molecular weights. We want to address that we synthesized relatively high molecular weight (~200000 of Mn) polymers for both pristine and Si-analogue to enhance charge carrier mobility. In the cases of lower molecular weights, although overall solubility is enhanced, similar trend was observed and more importantly, the highest semiconductor performances were obtained from high molecular weight. In other words, the difference in solubility is primarily caused by structural changes rather than either differing molecular weights. In addition, as shown from contact angle measurements in Figure 2.1d, SiDPP-TVT exhibited higher hydrophobicity than DPP-TVT; SiDPP-TVT and DPP-TVT had 23.64 mN m-1 and 27.67 mN m-1 of surface energy, respectively (Table 2.1).[24]
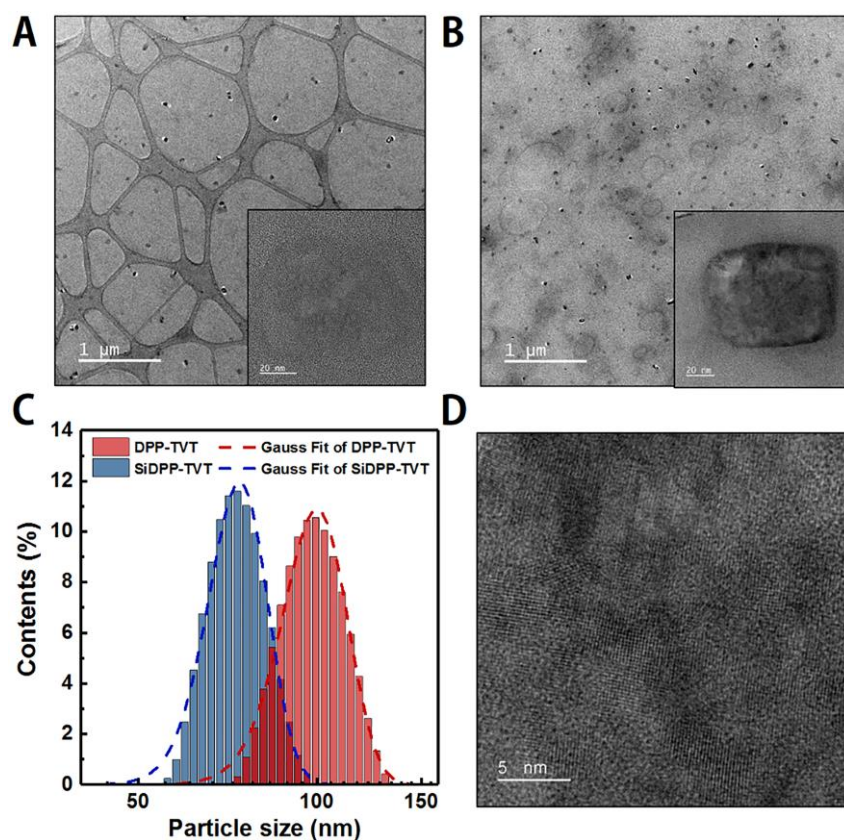
Figure 2.2 HR-TEM image of (a) DPP-TVT and (b) SiDPP-TVT. (c) The DLS measurement results of particle size distribution of DPP-TVT and SiDPP-TVT using mini-emulsion synthesis. (d) The magnified HR-TEM image of a SiDPP-TVT colloidal particle surface.

Table 2.1 Summary of contact angle, calculated surface energy and DLS measurements results in mini-emulsion synthesis.

Polymer	Contact angle (°)		Surface energy	Z-Ave.[a]	PDI
	water	diiodomethane	$(mN\ m^{-1})$	(nm)	
DPP-TVT	102.0	62.1	27.67	97.51	0.565
SiDPP-TVT	104.2	68.9	23.64	72.40	0.486

[a] Average particle size of each colloid measured by DLS method.

In order to investigate the effect of high solubility and hydrophobicity of newly synthesized SiDPP-TVT on the mini-emulsion synthesis, high-resolution transmission electron microscopy (HR-TEM) measurements were carried out for each colloid and the results are shown in Figure 2.2. The sizes of the water-borne colloidal particles synthesized from DPP-TVT and SiDPP-TVT can be compared. The actual particle size of the HR-TEM image in Figures 2.2a and 2b is consistent with the average particle size measured from DLS analyses conducted in colloids shown in Figure 2.2c. For example, enlarged image of a single colloid particle of the SiDPP-TVT in Figure 2.2b is about 78 nm, which is similar to the Z-average value of the DLS results. As shown in Figure 2.2d, further investigation of TEM images shows well-aligned lamellar crystalline structure of SiDPP-TVT is well-preserved within colloid particles. When comparing the statistical size of water-borne colloid particles, SiDPP-TVT and DPP-TVT demonstrated Z-average values of 72.40 nm and 97.51 nm, respectively. Moreover, the SiDPP-TVT and the DPP-TVT exhibited polydispersity index (PDI) of 0.486 and 0.565, respectively, indicating that the SiDPP-TVT formed more uniform colloids. Collectively, the TEM and DLS results of the two polymers indicate that SiDPP-TVT forms a smaller and more uniform particle size than DPP-TVT, which is evidences of more efficient mini-emulsion synthesis when SiDPP-TVT is employed. We address that such improved emulsification efficiency can be attributed to increased solubility and hydrophobicity of SiDPP-TVT.

2.2. Film Morphology
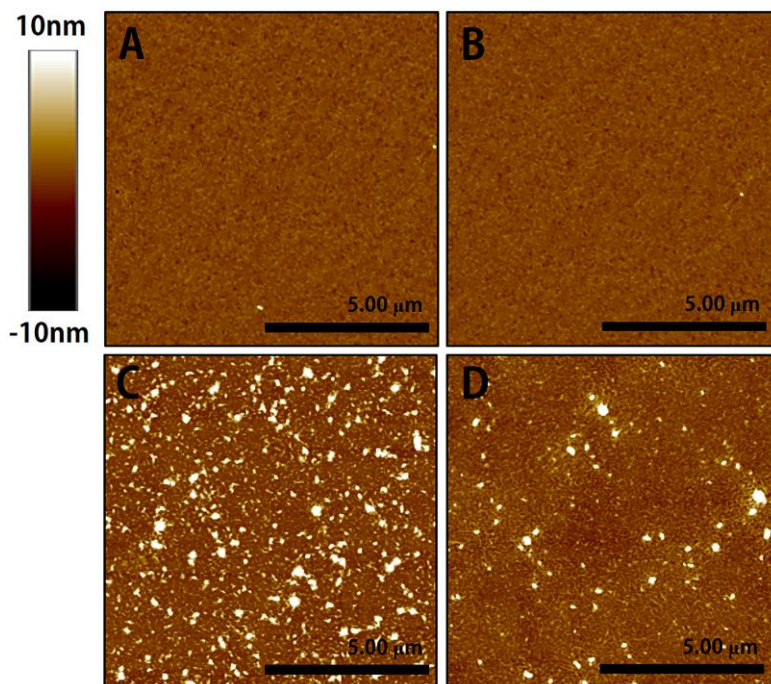
Figure 2.3 AFM images of (a) DPP-TVT using chloroform, (b) SiDPP-TVT using chloroform, (c) DPP-TVT using water and (d) SiDPP-TVT using water. (In the case of thin films realized by mini-emulsion synthesis, they were post-treated to remove residual surfactants.)

Table 2.2 Film roughness and 2D-GIXD parameters.

Polymer film	Rq (nm)	π-π stacking distance (Å)	d-spacing (Å)	$g_{(010)}$ (%)	$g_{(l00)}$ (%)
DPP-TVT (chloroform)	0.689	3.68	27.22	8.12	4.12
SiDPP-TVT (chloroform)	0.643	3.67	28.39	8.45	3.86
DPP-TVT (water)	2.748	3.64	27.18	8.51	4.36
SiDPP-TVT (water)	1.113	3.66	29.41	8.48	3.92

As described earlier, these small and uniform water-borne colloids of SiDPP-TVT might facilitate very even coalescence phenomenon during solidification or film formation. We investigated the actual morphology of thin films cast from water-borne colloids of two polymers by using an atomic force microscope (AFM) and a scanning electron microscope (SEM). Here, all the fabricated thin films from colloids were washed with pure ethanol to remove residual surfactants as previously reported.[11] To examine the effects of the post-treatment on the removal of residual surfactants, we performed Fourier Transform-Infrared Spectroscopy (FT-IR) analyses. Cetyltrimethylammonium bromide (CTAB), a surfactant used in this study, can be characterized by both the C-N bond in the amine head group and the long alkyl chain in the tail group; the C-N bond in the alpha and beta peaks and the peaks for the C-H bonds in the long alkyl chains in gamma peaks.[25, 26] After the post-treatment of ethanol washing, we confirmed these peaks were reduced significantly in both polymer semiconductors and becomes similar to those films cast from chloroform. As shown in Figures 2.3a and b, topology of the films of DPP-TVT and SiDPP-TVT cast from chloroform are very smooth with r.m.s. roughness of 0.689 nm and 0.643 nm, respectively, typical for good organic solvent-based films. Figure 2.3c corresponding to topology of films cast from colloid of DPP-TVT shows much more pronounced morphological features with r.m.s. roughness of 2.748 nm. In the case of colloids of SiDPP-TVT, the fabricated thin film rendered much smoother morphology with r.m.s. roughness of 1.113 nm, comparable to the cases of organic solvents. This trend is similarly observed from large-scale SEM images, where the DPP-TVT film cast from colloid had significantly more aggregated morphologies than the case of SiDPP-TVT. We want to address that this is the first observation of topology images of films cast from polymer semiconductor colloids comparable to that cast from organic solvents, especially when high mobility, planar backboned polymer semiconductors are used. It seems that more efficient coalescence occurs when using colloids of SiDPP-TVT because of its relatively higher emulsification efficiency. This is enabled by not only initially smaller particle size but also narrow size distribution of SiDPP-TVT colloid, which inhibited inter-particle aggregation when solvent was evaporating rapidly for solidification. As a result, we believe that coalescence can be ideally realized when films are fabricated from SiDPP-TVT colloids.

2.3. Crystallinity and Molecular Orientation

We conducted 2-Dimensional Grazing Incidence X-ray Diffraction (2D-GIXD) analyses to study the molecular-level disorder, crystallinity, and orientation affecting the charge transport. All the polymer films cast from both chloroform solution and water-borne colloids showed highly oriented edge-on structures, with well-developed Bragg diffraction peaks of up to (004) in the q_z direction (Figure 2.4).
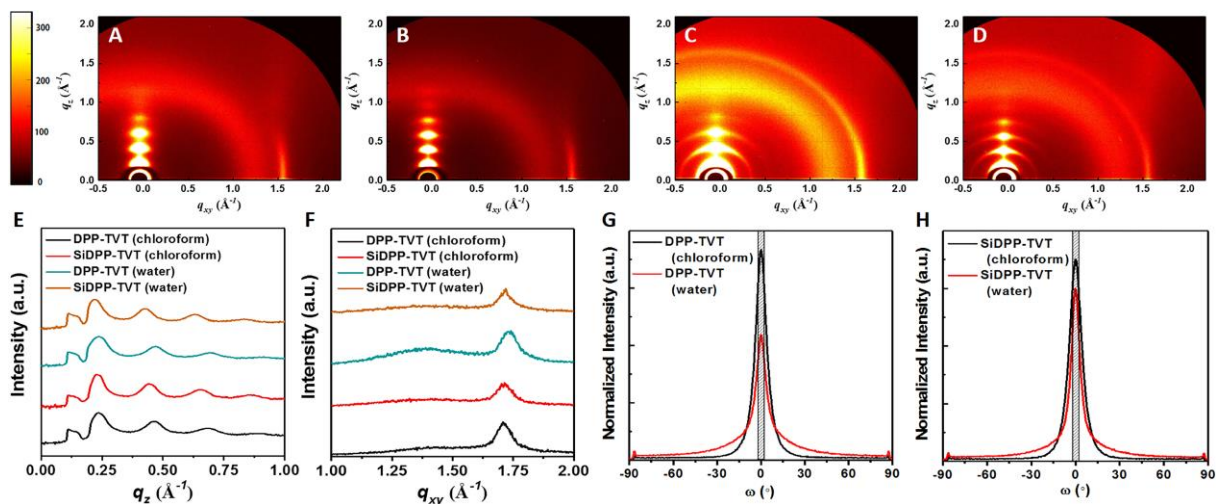
Figure 2.4 2D-GIXD patterns measured from (a) DPP-TVT film (chloroform), (b) SiDPP-TVT film (chloroform), (c) DPP-TVT film (water), (d) SiDPP-TVT film (water) and their corresponding extracted profiles along (e) with q_z direction and (f) q_{xy} direction. The pole figures for each film normalized by (200) scattered intensity (g) with DPP-TVT film and (h) with SiDPP-TVT film.

In the cases of thin films cast from chloroform, the π-π stacking distances of DPP-TVT and SiDPP-TVT were very similar as 3.68 Å and 3.67 Å, respectively (Table 2.2). However, in the case of d-spacing, the DPP-TVT stacking distance was apparently shorter by 1.17 Å compared to that of SiDPP-TVT of 28.39 Å. This can be attributed to the increased volumetric portion of alkyl solubilizing group of SiDPP-TVT as a result of silicon substitution. In the case of the thin films cast from water-borne colloids, more dispersed ring-like patterns appeared in each Bragg diffraction spot, indicating lower degree of edge-on orientation. To more quantitatively investigate the relative edge-on orientation of polymer semiconductors with different processing solvents, we conducted pole figure analyses based on angular distribution of (200) diffraction peaks to avoid possible errors caused by reflected light. Due to the geometry of the 2D-GIXD experiment and the curved surface of the Ewald sphere, the detector angle is not exactly matched with polar angle (ω). At q ≈ 0.42 Å^{-1} ((200) diffraction peaks), the zero angle of detector plane corresponds to |ω| ≈ 2.15 °, so we cannot obtain the intensity information for the orientation |ω| < 2.15 °.[27-29] The inaccessible ω area is designated by gray-pattern region in Figures 2.4g and h. As clearly summarized in Figures 2.4g and h, in each polymer, thin film cast from chloroform solution showed more preferred edge-on orientation compared to the case of water-borne colloid. However, it should be noted that the relative difference in degree of edge-on orientation becomes significantly smaller in Figure 2.4h, where SiDPP-TVT is used, which can be attributed to more efficient coalescence phenomenon even when processed

from water-borne colloids. From GIXD data, it is also possible to calculate paracrystalline disorder which is related with the degree of crystalline perfectness. The paracrystalline disorder parameter ($g_{(l00)}$) of polymer films for q_z direction can be calculated from the slope of a δb–h^2 plot extracted from 2D-GIXD data, where the slope (m) of the δb–h^2 plot is determined by:

$$m = \frac{g_{(l00)}^2 \pi^2}{d} ,$$ (4)

where d is the domain spacing, δb is the integral widths of the diffraction peaks, and h is the order of diffraction.[28] The paracrystalline disorder can be also analyzed for the q_{xy} direction by using the single peak-width estimation method based on a single (010) peak,

$$g_{(010)} = \sqrt{\frac{\Delta q}{2\pi q_0}} ,$$ (5)

where $g_{(010)}$ is the paracrystalline disorder in the q_{xy} direction, Δq is the breadth of the diffraction peak, and q_0 is the center position of the peak.[29] All the obtained paracrystalline disorder values are summarized in Table 2.2. In both paracrystalline disorders of q_z and q_{xy}, interestingly, exactly the same trend is observed; disorders of the polymer films become slightly higher when cast from water-borne colloids compared to the case of chloroform and SiDPP-TVT that always resulted in smaller differences between chloroform and water-borne colloid. Therefore, one can see that more efficient emulsification efficiency of SiDPP-TVT enabled better crystalline orientation as well as crystallinity when polymer chains are self-assembled during solidification. This is in accordance with the experimental observation in morphology session.

2.4. Electrical Properties of Organic Field-effect Transistors (OFETs)
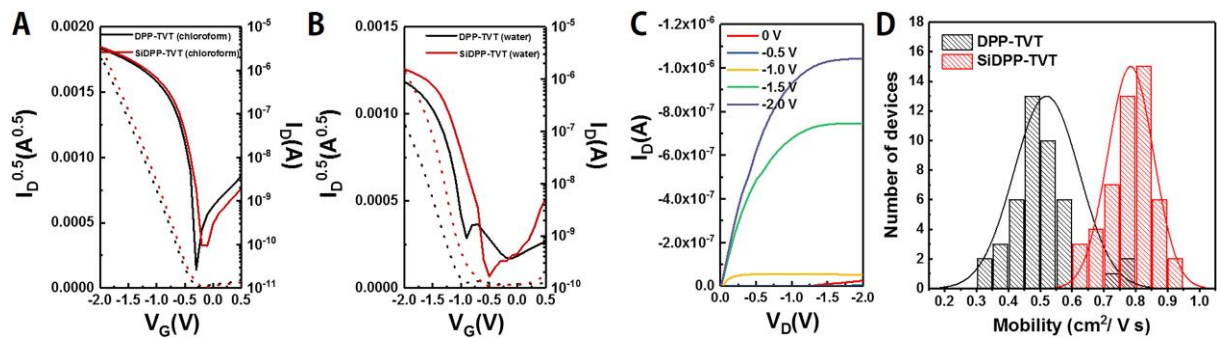
Figure 2.5 The transfer curves of (a) chloroform based devices and (b) water based devices. (c) The output characteristics of water based devices using SiDPP-TVT. (d) Device-to-device deviation of charge carrier mobility comparison in DPP-TVT and SiDPP-TVT using mini-emulsion synthesis.

Table 2.3 Summary of electrical properties of OFETs.

	μ_{max} (cm²V⁻¹s⁻¹)	μ_{ave}[a] (cm²V⁻¹s⁻¹)	V_{th} (V)	$I_{D,max.}$ (μA)	on/off ratio	N_{tr} (cm⁻²)
DPP-TVT (chloroform)	0.98	0.94±0.06	-0.32±0.04	3.22	10^5	$6.79×10^{11}$
SiDPP-TVT (chloroform)	1.01	0.97±0.05	-0.21±0.04	3.47	10^5	$4.46×10^{11}$
DPP-TVT (water)	0.76	0.51±0.12	-0.96±0.07	0.92	10^3	$2.04×10^{12}$
SiDPP-TVT (water)	0.91	0.78±0.08	-0.54±0.05	1.67	10^4	$1.15×10^{12}$

[a] Average values were obtained from 50 independent devices.

We conducted experiments on low-operating voltage, high reliability devices to account for the recent issue of FET-device electrical parameter extraction errors. These include both overestimated mobility values extracted from kinks as well as kinks that are caused by high-bias operation.[30, 31] To determine electrical properties that are appropriate for OFETs, we fabricated their bottom-gate/top-contact geometry using high-k dielectric materials, ZrO_x, via the sol-gel method. In particular, we chose bottom-gate/top contact-geometry to ensure that the difference in electrical parameters can be clearly explained by the difference in morphology and crystalline structure. The source-drain channel lengths were designed with sufficiently large (75-150 µm) to prevent short-channel effects.[30] As shown in Figure 2.5a, when chloroform was used, the highest charge carrier mobility calculated for the DPP-TVT was 0.98 cm² V⁻¹ s⁻¹, while for the SiDPP-TVT, it was a similar value of 1.01 cm² V⁻¹ s⁻¹ (Table 2.3). In the cases of FETs fabricated from water-borne colloids, it was found that the charge carrier mobility of the DPP-TVT decreased by about 46% from 0.94±0.06 cm² V⁻¹ s⁻¹ to 0.51±0.12 cm² V⁻¹ s⁻¹. Interestingly, the charge carrier mobility of SiDPP-TVT decreased only slightly from 0.97±0.05 cm² V⁻¹ s⁻¹ to 0.78±0.08 cm² V⁻¹ s⁻¹, approximately 19%. (Figure 2.5b). In overall, charge carrier mobility is decreased in the case of water-borne colloids compared to the cases of chloroform. This result is obvious when considering significant amount of trap states at the semiconductor/dielectric interfaces generated by solidification of water-borne colloids. Nonetheless, it is worth to note that SiDPP-TVT showed significantly smaller mobility decrease when solvents were changed from chloroform to water. The trap density in OFET geometry can be calculated using

$$N_{tr} = \frac{C_i V_{th}}{e} \quad ,$$
(6)

where N_{tr} is the trap density, C_i is the capacitance of the dielectric layer, V_{th} is the threshold voltage, and e is the charge of an electron.[32] We were able to approximate the room-temperature concentrations of the trap states of the DPP-TVT and the SiDPP-TVT processed from water-borne colloids as ~ 2.04×10^{12} and 1.15×10^{12} cm^{-2}, respectively. Therefore, we speculate that despite of colloid processes, morphological interfacial defects such as impurities and voids were much less generated in the case of SiDPP-TVT due to its higher coalescence efficiency. In order to confirm that SiDPP-TVT is more suitable for mini-emulsion synthesis than DPP-TVT, we tested their reliability by fabricating 50 independent FET devices and analyzed their statistical electrical parameters. As Figure 2.5d shows, the performance distribution of the independent devices, which can be expressed by full width at half maximum, becomes significantly narrower for SiDPP-TVT as 0.088 compared to 0.165 of DPP-TVT, indicating almost 2 times narrower distribution. Collectively, OFET studies showed that SiDPP-TVT, with remarkable solubility and hydrophobicity with surfactants, can be a promising candidate for water-borne semiconductors not only in terms of charge carrier mobility but also in terms of device-to-device reliability.

IV. Conclusion

From the perspective of improving mini-emulsion synthesis, we designed a new polymer semiconductor SiDPP-TVT with the aim of enhancing molecular affinity against ionic surfactants. Newly synthesized SiDPP-TVT was designed to possess high solubility and also high hydrophobicity without damaging the semiconductor properties of the reference polymer semiconductor, DPP-TVT, by replacing the branching C atom of the alkyl solubilizing group to Si atom. We show that SiDPP-TVT could result in small and uniform colloidal particles via mini-emulsion synthesis because of strengthened molecular affinity against surfactant and thus enhanced emulsification efficiency. Thanks to very efficient coalescence phenomenon driven by high quality colloidal solutions with small and uniform particles, we could show that fine thin film morphology as well as highly edge-on oriented, low disorder crystalline structure can be realized even from water-borne colloids. As a result, for the first time we show that the use of water-borne colloids of strategically designed polymer semiconductors can result in outstanding FET performances, even comparable to that of organic solvents.

V. References

[1]   Li, X., Wolanin, P.J., MacFarlane, L.R., Harniman, R.L., Qian, J., Gould, O.E., Dane, T.G., Rudin, J., Cryan, M.J., Schmaltz, T. and Frauenrath, H., 2017. Uniform electroactive fibre-like micelle nanowires for organic electronics. Nature communications, 8(1), pp.1-9.

[2]   Zhao, Y., Zhao, X., Roders, M., Gumyusenge, A., Ayzner, A.L. and Mei, J., 2017. Melt-Processing of Complementary Semiconducting Polymer Blends for High Performance Organic Transistors. Advanced Materials, 29(6), p.1605056.

[3]   Song, D., Mahajan, A., Secor, E.B., Hersam, M.C., Francis, L.F. and Frisbie, C.D., 2017. High-resolution transfer printing of graphene lines for fully printed, flexible electronics. ACS nano, 11(7), pp.7431-7439.

[4]   Jeong, H., Baek, S., Han, S., Jang, H., Kim, S.H. and Lee, H.S., 2018. Novel Eco-Friendly Starch Paper for Use in Flexible, Transparent, and Disposable Organic Electronics. Advanced Functional Materials, 28(3), p.1704433.

[5]   Landfester, K., Montenegro, R., Scherf, U., Güntner, R., Asawapirom, U., Patil, S., Neher, D. and Kietzke, T., 2002. Semiconducting polymer nanospheres in aqueous dispersion prepared by a miniemulsion process. Advanced Materials, 14(9), pp.651-655.

[6]   Darwis, D., Elkington, D., Ulum, S., Bryant, G., Belcher, W., Dastoor, P. and Zhou, X., 2013. Novel low voltage and solution processable organic thin film transistors based on water dispersed polymer semiconductor nanoparticulates. Journal of colloid and interface science, 401, pp.65-69.

[7]   Xie, C., Classen, A., Späth, A., Tang, X., Min, J., Meyer, M., Zhang, C., Li, N., Osvet, A., Fink, R.H. and Brabec, C.J., 2018. Overcoming microstructural limitations in water processed organic solar cells by engineering customized nanoparticulate inks. Advanced Energy Materials, 8(13), p.1702857.

[8]   Pedersen, E.B.L., Pedersen, M.C., Simonsen, S.B., Brandt, R.G., Böttiger, A.P., Andersen, T.R., Jiang, W., Xie, Z.Y., Krebs, F.C., Arleth, L. and Andreasen, J.W., 2015. Structure and crystallinity of water dispersible photoactive nanoparticles for organic solar cells. Journal of Materials Chemistry A, 3(33), pp.17022-17031.

[9]   Holmes, N.P., Marks, M., Kumar, P., Kroon, R., Barr, M.G., Nicolaidis, N., Feron, K., Pivrikas, A., Fahy, A., de Zerio Mendaza, A.D. and Kilcoyne, A.D., 2016. Nano-pathways: bridging the divide between water-processable nanoparticulate and bulk heterojunction organic photovoltaics. Nano Energy, 19, pp.495-510.

[10]   Cho, J., Cheon, K.H., Ahn, H., Park, K.H., Kwon, S.K., Kim, Y.H. and Chung, D.S., 2015. High Charge-Carrier Mobility of 2.5 cm2 V− 1 s− 1 from a Water-Borne Colloid of a Polymeric Semiconductor via Smart Surfactant Engineering. Advanced Materials, 27(37), pp.5587-5592.

[11]   Cho, J., Yoon, S., Sim, K.M., Jeong, Y.J., Park, C.E., Kwon, S.K., Kim, Y.H. and Chung, D.S., 2017. Universal selection rule for surfactants used in miniemulsion processes for eco-friendly and high performance

polymer semiconductors. Energy & Environmental Science, 10(11), pp.2324-2333.

[12]   Sarrazin, P., Chaussy, D., Vurth, L., Stephan, O. and Beneventi, D., 2009. Surfactant (TTAB) Role in the Preparation of 2, 7-Poly (9, 9-dialkylfluorene-co-fluorenone) Nanoparticles by Miniemulsion. Langmuir, 25(12), pp.6745-6752.

[13]   Kang, I.L., Yun, H.J., Chung, D.S., Kwon, S.K. and Kim, Y.H., 2013. Record high hole mobility in polymer semiconductors via side-chain engineering. Journal of the American Chemical Society, 135(40), pp.14896-14899.

[14]   Lu, C., Chen, H.C., Chuang, W.T., Hsu, Y.H., Chen, W.C. and Chou, P.T., 2015. Interplay of molecular orientation, film formation, and optoelectronic properties on isoindigo-and thienoisoindigo-based copolymers for organic field effect transistor and organic photovoltaic applications. Chemistry of Materials, 27(19), pp.6837-6847.

[15]   Guo, X., Ortiz, R.P., Zheng, Y., Kim, M.G., Zhang, S., Hu, Y., Lu, G., Facchetti, A. and Marks, T.J., 2011. Thieno [3, 4-c] pyrrole-4, 6-dione-based polymer semiconductors: toward high-performance, air-stable organic thin-film transistors. Journal of the American Chemical Society, 133(34), pp.13685-13697.

[16]   Melkonyan, F.S., Zhao, W., Drees, M., Eastham, N.D., Leonardi, M.J., Butler, M.R., Chen, Z., Yu, X., Chang, R.P., Ratner, M.A. and Facchetti, A.F., 2016. Bithiophenesulfonamide building block for π-conjugated donor–acceptor semiconductors. Journal of the American Chemical Society, 138(22), pp.6944-6947.

[17]   Sung, M.J., Luzio, A., Park, W.T., Kim, R., Gann, E., Maddalena, F., Pace, G., Xu, Y., Natali, D., de Falco, C. and Dang, L., 2016. High-Mobility Naphthalene Diimide and Selenophene-Vinylene-Selenophene-Based Conjugated Polymer: n-Channel Organic Field-Effect Transistors and Structure–Property Relationship. Advanced Functional Materials, 26(27), pp.4984-4997.

[18]   Jones, R.G., Ando, W. and Chojnowski, J. eds., 2013. Silicon-containing polymers: the science and technology of their synthesis and applications. Springer Science & Business Media.

[19]   Davidson, G., 1993. Spectroscopic properties of inorganic and organometallic compounds (Vol. 26). Royal Society of chemistry.

[20]   Tiab, D. and Donaldson, E.C., 2015. Petrophysics: theory and practice of measuring reservoir rock and fluid transport properties. Gulf professional publishing.

[21]   Asakura, S. and Oosawa, F., 1954. On interaction between two bodies immersed in a solution of macromolecules. The Journal of chemical physics, 22(7), pp.1255-1256.

[22]   Bonard, J.M., Stora, T., Salvetat, J.P., Maier, F., Stöckli, T., Duschl, C., Forró, L., de Heer, W.A. and Châtelain, A., 1997. Purification and size-selection of carbon nanotubes. Advanced Materials, 9(10), pp.827-831.

[23]   Sun, W., 2014. Interaction forces between a spherical nanoparticle and a flat surface. Physical Chemistry Chemical Physics, 16(12), pp.5846-5854.

[24]   Effertz, C., Lahme, S., Schulz, P., Segger, I., Wuttig, M., Classen, A. and Bolm, C., 2012. Design of Novel Dielectric Surface Modifications for Perylene Thin-Film Transistors. Advanced Functional Materials, 22(2), pp.415-420.

[25]   Socrates, G., 2004. Infrared and Raman characteristic group frequencies: tables and charts. John Wiley & Sons.

[26]   Larkin, P., 2017. Infrared and Raman spectroscopy: principles and spectral interpretation. Elsevier.

[27]   Rivnay, J., Mannsfeld, S.C., Miller, C.E., Salleo, A. and Toney, M.F., 2012. Quantitative determination of organic semiconductor microstructure from the molecular to device scale. Chemical reviews, 112(10), pp.5488-5519.

[28]   Baker, J.L., Jimison, L.H., Mannsfeld, S., Volkman, S., Yin, S., Subramanian, V., Salleo, A., Alivisatos, A.P. and Toney, M.F., 2010. Quantification of thin film crystallographic orientation using X-ray diffraction with an area detector. Langmuir, 26(11), pp.9146-9151.

[29]   Rivnay, J., Noriega, R., Kline, R.J., Salleo, A. and Toney, M.F., 2011. Quantitative analysis of lattice disorder and crystallite size in organic semiconductor thin films. Physical Review B, 84(4), p.045203.

[30]   Choi, H.H., Cho, K., Frisbie, C.D., Sirringhaus, H. and Podzorov, V., 2017. Critical assessment of charge mobility extraction in FETs. Nature materials, 17(1), p.2.

[31]   McCulloch, I., Salleo, A. and Chabinyc, M., 2016. Avoid the kinks when measuring mobility. Science, 352(6293), pp.1521-1522.

[32]   Podzorov, V., Menard, E., Borissov, A., Kiryukhin, V., Rogers, J.A. and Gershenson, M.E., 2004. Intrinsic charge transport on the surface of organic semiconductors. Physical review letters, 93(8), p.086602.

[33]   Yu, S.H., Park, K.H., Kim, Y.H., Chung, D.S. and Kwon, S.K., 2017. Fine molecular tuning of diketopyrrolopyrrole-based polymer semiconductors for efficient charge transport: effects of intramolecular conjugation structure. Macromolecules, 50(11), pp.4227-4234.

[34]   Park, Y.M., Desai, A., Salleo, A. and Jimison, L., 2013. Solution-processable zirconium oxide gate dielectrics for flexible organic field effect transistors operated at low voltages. Chemistry of Materials, 25(13), pp.2571-2579.

[35]   Park, Y.M., Daniel, J., Heeney, M. and Salleo, A., 2011. Room-temperature fabrication of ultrathin oxide gate dielectrics for low-voltage operation of organic field-effect transistors. Advanced Materials, 23(8), pp.971-974.

Part 3. Breath-Figure Molding of Polymer Transistors to Implement Flexible and High-Performance NO_x Sensors

I. Introduction

Due to growing interest in personal air quality monitoring and breath analysis, industrial demand for accurate and sustainable gas sensors to detect various gases is rapidly increasing. In particular, coupled with the technology of Internet of Things (IoT), it is necessary to develop low-power flexible gas sensors with selectivity for specific gas analytes.[1–9] Examples of typical commercially available gas sensors include metal oxide-based gas sensors, which operate on the principle of changes in resistance due to gas-oxide redox reactions at high temperatures; however, these are not suitable as sustainable IoT gas sensors because of additional energy needed for operating/ensuring high-performance of gas sensors.[10–13] In this regard, organic semiconductors (OSCs) have been studied extensively as alternative materials that meet the requirements of next-generation gas sensors such as low cost, low power, and flexibility.[8,9,14–27] In particular, organic field effect transistors (OFETs) have been found to be capable of overcoming the limitations imposed by size, power consumption, and sensitivity.[8,9,14–19,21–26] When exposed to a gas, the density-of-states of an OSC undergoes changes depending on the reducing/oxidizing nature of each gas analyte, resulting in modulations in the channel current. Because this operating mechanism is not a Brønsted redox reaction, a high operating temperature is not required and operation at low power levels is possible.[8,12,14,23] Nonetheless, owing to a lack of direct redox reactions, OFET gas sensors exhibit a relatively low gas sensitivity, which limits their commercial applications.

Recently, several smart strategies have been developed to enhance the sensitivity of OFET and other OSC gas sensors, including 1) modifying the morphology to increase the contact area between gas molecules and active layer,[8,14–20] 2) minimizing the sensing layer thickness,[9,21,22] 3) controlling charge carrier concentration in the materials,[23] and 4) blending with a gas receptor material.[24–27] Though these approaches have been successful in delivering significantly enhanced sensitivity (as high as that of metal-oxide gas sensors), it should be noted that most of these methods employed small molecule semiconductors. This is because as seen in the case of an organic single crystal gas sensor, the morphology and thickness of small molecule semiconductors are easier to control than those of polymer semiconductors. However, the use of small molecule semiconductors does not take full advantage of the solution-processability/flexibility characteristics of OSCs, which is not suitable for low cost, wearable and portable IoT gas sensors. In this regard, solution-processable polymer semiconductors can be a perfect fit for developing next-generation gas sensors. Unfortunately, so far all the reported polymer gas sensor rendered worse sensing ability compared to the cases of small molecular semiconductor,

presumably due to difficulties in direct and dramatic morphology control for enhancing sensitivity of polymer semiconductors.[14,15,17,21,23] Nevertheless, there are a few attempts to maximize gas-exposure area in polymer semiconductors by inducing phase separation in a polymer dielectric and achieve porosity.[8] However, in this case, there is a limitation of conserving charge transport characteristics due to indirect morphology control of polymer semiconductors.

Another notable limitation faced by previously reported OSC gas sensors is that most of these studies have been focused on NH_3 or NO_2.[8,9,14–19,21,23,25,26] NO_x, which is mainly generated as a by-product of thermal power generation or vehicles, has been classified in 1990 as one of the six mandated criteria pollutants in Clean Air Act regulations.[28] NO_x may refer to various compounds such as NO, NO_2, and N_2O; of these, NO and NO_2 account for the majority.[29] Most of the studies on OSC NO_x gas sensors have focused on NO_2 gas alone with very few paying attention to NO. This is because the NO_2 molecule has a stronger electron withdrawing property than the NO molecule and is thus easier to detect.[30–32] To address this research gap, in the present study, though we conducted an overall analysis for various gas analytes, we primarily focused on NO.

In this investigation, we employed the Breath-Figure (BF) molding method to fabricate gas-readable polymer semiconductors with high sensitivity and selectivity at room temperature. In this method, a polymer semiconductor itself was used as the receptor that interacts with gas analytes as well as the charge transport layer responsible for signal transport. Based on comparative studies on various polymer semiconductors, we show that donor-acceptor copolymers are good receptors for reducing and oxidizing gas analytes. Furthermore, BF molding of donor-acceptor copolymers results in a highly reproducible porous morphology and maximizes the gas-exposure area. Interestingly, the "polymer-bag" effect of BF molding enables mostly conserved charge carrier mobility of BF-modified film compared to the pristine film, which guarantees fast signal transport.[33–36] Optimized BF-molded poly(2,5-{2-octyldodecyl}-3,6-diketopyrrolopyrrole-alt-5,5-{2´,5´-di[thien-2-yl]thieno[3,2-b]thiophene}) (DPP-DTT) was used to fabricate high-performance NO gas-sensing OFETs with a maximum sensitivity of 774%/ppm and a low limit of detection (LOD) of 110 ppb. Because such BF-OFETs exhibit reversed polarity of sensitivity against reducing gases and a far lower sensitivity against other less polar volatile organic compounds (VOCs), they can be used in universal gas-detection kits, especially for NO_x gases. Furthermore, we demonstrate flexible BF-OFETs fabricated on plastic substrates, which exhibited excellent flexibility as confirmed their sensitivity (500.93%/ppm) and LOD (215 ppb), and responsivity degradation of only 14.2% after 10,000 bending cycles at a 1% strain.

II. Experimental Section

2.1 Device fabrication

P3HT, PBTTT, DPP-DTT, and PPDT2FBT-DTT were purchased from Rieke Metals, Sigma Aldrich, Ossila, and 1-Material respectively, and used without further purification. Highly n-doped Si^{++}/SiO_2 (100 nm) wafers were used as substrate/gate for conventional devices. Si wafers were cleaned using a piranha solution and oxygen plasma. All the polymers were dissolved in chloroform at a concentration of 3 mg mL^{-1}. Subsequently, these solutions were aged for several days to facilitate the formation of stable ordered microdroplets.[36] In the next step, aged polymer solutions were spin-coated at 2000 rpm for 3–30 s on chosen substrates. To fabricate BF-molded polymer films, a short spin-coating time of less than 5 s was set to allow water condensation and evaporation. For BF molding, the temperature of the glove box was kept at 23–25 °C and the relative humidity was adjusted to 52%–88% to control pore size at the desired level. In the case of reference films, fabrication was conducted in a N_2-filled glove box. To obtain high-performance OFETs, P3HT, PBTTT, DPP-DTT, and PPDT2FBT-DTT films were annealed at 150, 175, 200, and 200 °C, respectively, for 20 min. Au source and drain electrodes (80 nm) were deposited on the polymer semiconductor layer by thermal evaporation at an evaporating rate of 0.2 Å s^{-1} with a channel and width of 150 and 1500 μm respectively. Polyimide (~125 μm) substrates were used to fabricate flexible sensors and crosslinked PVP was coated on the polyimide substrate as a smoothing layer. In the next step, an Ag gate electrode (50 nm) was deposited on the polyimide substrate by thermal evaporation at an evaporation rate of 0.2 Å s^{-1}. To prepare PVP solutions, PVP (Sigma Aldrich, M_w ~25,000) was initially mixed with 10 wt.% propylene glycol monomethyl ether acetate and to this mixture, a cross-linking agent, poly(melamine-co-formaldehyde), was added. The obtained PVP solution was spin-coated at 3000 rpm for 60 s and subsequently crosslinked for 3 h at 150 °C in a vacuum oven. The thickness of the resulting PVP dielectric layer was 460 nm and its areal capacitance was 9.2 nF cm^{-2}.[44,45] Subsequent polymer film and electrode deposition processes were similar to the method used for fabricating Si substrate-based devices.

2.2 Film characterization

To analyze the surface morphology of the fabricated OFETs, atomic force microscopy (Park Systems, XE-150) and scanning electron microscopy (Hitachi, SU8230) were conducted. GIXD measurements were performed at the PLS-II 3C and 9A beamlines at the Pohang Accelerator Laboratory (PAL) in Korea. All the films were manufactured in the same manner that the devices were fabricated. Capacitance of the dielectric layers was measured using a Keysight E4981 capacitance meter operating at 1 kHz.

2.3 Measurements

The electrical characteristics of the devices were measured using a parameter analyzer (Agilent Technologies, B1500A) in a test chamber on a probe station at standard relative humidity and temperature condition. Charge carrier mobilities were calculated from the equation $\Delta I_{DS} = \frac{W C_i \mu}{2L} (V_{GS} - V_{th})^2$, where I_{DS} is the source-drain current, C_i is the capacitance per unit area of the dielectric layer, μ represents mobility, W and L are the channel width and length, and V_{GS} and V_{th} are the gate voltage and threshold voltage, respectively.[40] To analyze the gas sensing properties of the sensors, N_2 and other gases (100 ppm standard gases of NO, NO_2, NH_3, acetone, and ethanol and 1000 ppm standard gas of H_2) were mixed and tested at specific concentrations. The concentration of each gas was controlled using mass flow controllers. For gases other than N_2, the flow rate was 20 sccm while that of N_2 was 100–1000 sccm. The following gas dilution equation was used to adjust gas concentration.

$$X_{Bi} = \frac{X_{B1} \times q_{span} + X_{B2} \times q_{dil}}{q_{span} + q_{dil}}$$

(4)

Here, X_{Bi} is the amount of substance fraction B in dilution i, q_{span} is the volume flow of the span gas, and q_{dil} is the volume flow of the dilution gas.[46].

III. Results and Discussion

To pick up polymer semiconductors with optimized gas receptor properties, initially, we tested the gas sensing behavior of bottom-gate (Si^{++}/SiO$_2$ 100 nm)/top-contact (Au) OFETs with spin-coated poly(3-hexylthiophene-2,5-diyl) (P3HT), poly[2,5-bis(3-tetradecylthiophen-2-yl)thieno[3,2-b]thiophene] (PBTTT),

DPP-DTT, and poly[(2,5-bis(2-hexyldecyloxy)phenylene)-alt-(5,6-difluoro-4,7-di(thiophen-2-yl)benzo[c]-[1,2,5]thiadiazole)] (PPDT2FBT-DTT) as active layers. Each active layer was constructed by simple spin-coating from chloroform with a thickness of ~40 nm. The chemical structures of these polymers and their corresponding transfer curves and responsivities upon exposure to 10 ppm NO are illustrated in Figure 3. Because NO is an oxidizing gas with electron-withdrawing properties, NO adsorption onto p-type polymer semiconductors results in an increased channel current, similar to the hole doping mechanism.[14,23,30] All p-type OFETs showed positively shifted transfer curves upon NO exposure, which is typical of p-doping. Interestingly, when we consider the shift in threshold voltage (ΔV_{th}), it is clear that donor-acceptor polymers, i.e., DPP-DTT and PPDT2FBT-DTT exhibit a much more pronounced shift when compared to the homopolymers P3HT and PBTTT. A similar but more pronounced trend is observed upon NO_2 exposure, a gas with stronger oxidizing and electron-withdrawing properties. The observed overall better performance of donor-acceptor copolymers over homopolymers for NO_x sensing can be related to the presence of the relatively larger dipole moment of the repeating units of donor-acceptor polymers in comparison to that of homopolymers. In other words, oxidizing gas analytes with strong electron-withdrawing properties interact strongly with polymer semiconductors with donor-acceptor moieties via efficient dipole-dipole interaction, resulting in a pronounced current modulation for its OFET gas sensor application.

Figure 3.1 (a) Polymer semiconductor selection criteria for high-performance OSC gas sensor, and the chemical structures of the polymer semiconductors used in this study. (b) The scheme of BF molding of polymer semiconductor films and final device structure. (c–f) The top row shows SEM top-view images of the fabricated polymer films, the middle row shows the corresponding AFM topographical images, and the bottom row shows the corresponding GIXD patterns. From the left, polymer films corresponding to these images are pristine, BF-S, BF-M, and BF-L DPP-DTT, respectively. (g) Pore size distribution of each BF molding film. (h) Line cut profiles extracted from AFM images to confirm actual pore size and height. (i) Transfer curves of pristine, BF-S, BF-M, and BF-L films exposed to N_2. (j) Responsivities of BF molding devices calculated from transfer curves

corresponding to N$_2$ and 10 ppm NO exposure. The shaded region indicates a V$_{GS}$ below V$_{th}$.

Though both DPP-DTT and PPDT2FBT-DTT show the possibility of gas sensing, their figures-of-merit, such as responsivity (defined as $\Delta I/I_0$ with $\Delta I = I_{gas}–I_0$, where I_{gas} and I_0 are the drain currents of gas-exposed and unexposed OFETs, respectively) and sensitivity (defined as the slope of the linear relationship of responsivity versus gas concentration), were far lower than those of small molecule gas sensors, presumably due to limited gas-exposure areas.[23] To overcome this issue, we adopted the BF molding method to fabricate OFETs of DPP-DTT and PPDT2FBT-DTT (Figure 3.1b). In BF molding, a polymer is dissolved in a low boiling-point solvent and cast on a substrate in high humidity conditions.[33–36] Spontaneous evaporation of the volatile solvent reduces the temperature of the upper surface of the solution and water droplets condense on its surface. These microdroplets grow with time and when they come in contact with other droplets, coalescence may occur. It is known that the "polymer-bag" effect, i.e., the encapsulation of water droplets by a thin polymer stratum can prevent microdroplets from coalescing with each other.[33] Consequently, these uniformly sized water droplet microspheres arrange themselves in a hexagonal pattern, resulting in a polymer imprint with a honeycomb pattern. In the present study, polymer semiconductors were employed for BF molding and their self-assembly behavior was found to dramatically influence the BF pattern shape and size. Cotlet et al. previously showed that BF molding can result in successful hexagonal patterns when polythiophene is dissolved in a good solvent and aged for several days, as such aggregates hinder coalescence and allow the formation of stable ordered microdroplets.[36] Similarly, the degree of crystallinity of a polymer can affect the BF pattern; highly crystalline polymers result in a greater "polymer-bag" effect and produce finer BF patterns. In this regard, DPP-DTT, with its greater degree of crystallinity, is better than PPDT2FBT-DTT. Another experimental detail for realizing successful BF pattern is that the thickness of polymer layer should not very thin, because water droplet size typically exceeds several hundreds of nm. For example, previously demonstrated perfect hexagonal BF patterns were typically obtained using drop casting in constant air-flow condition with significant thicknesses over 1 μm.[36] However, note that for gas sensor application, we should realize thin film thickness to synchronize gas receptor role and charge transport role of polymer semiconductor because charge transport of OFET occurs through a few tens of nm from the dielectric interface. Therefore, in the present study, we focused on realizing sufficiently porous and thin polymer semiconductor films using the BF method and not on the well-ordered hexagonal pattern.[35] In the case of spin-casted thin films of DPP-DTT (~40 nm), we could not observe well-defined hexagonal pattern, but more randomly distributed pores. In addition, in the case of PPDT2FBT-DTT, it was not easy to

control BF morphology owing to its lower crystallinity, which weakens the "polymer-bag" effect. By systematically controlling the humidity and air flow conditions for BF molding, we could realize three kinds of thin films (40–50 nm); these include DPP-DTT: BF-L with a large pore size (2.03±1.31 μm), BF-M with a medium pore size (747±520 nm), and BF-S with a small pore size (293±387 nm) (Figure 3.1). In the case of BF-L and BF-M, pores touched the dielectric interface while in the case of BF-S, the dielectric surface was fully covered with the polymer. The root-mean-square (rms) roughness values corresponding to BF-L, BF-M, BF-S, and pristine films were 17.40, 11.83, 2.44, and 0.90 nm, respectively.

Although the BF technology can ensure a large gas-exposure area, at the same time, it can perturb charge transport, which is detrimental to the performance of gas sensors. To study the crystalline orientation of BF-L, BF-M, and BF-S DPP-DTT films and compare them with that of the pristine DPP-DTT film, grazing incident X-ray diffraction (GIXD) analysis was conducted. As shown in Figure 3.1, on the whole, the GIXD patterns of BF-modified polymer films were similar to that of the non-modified pristine DPP-DTT film. To investigate the crystallinity of polymer films quantitatively, paracrystalline disorder (g) analysis was conducted. The relationship between paracrystalline disorder and crystallinity is given by

$$g = \sqrt{\frac{\Delta q}{2\pi q_0}}$$

$$(1)$$

where Δq and q_0 are the width and center, respectively, of the corresponding diffraction peak.[37–39] We calculated the paracrystalline disorder of the (010) diffraction peak along the in-plane direction. Details on the calculation of $g_{(010)}$ can be found in the supporting information; the calculated $g_{(010)}$ values were 12.62%, 12.70%, 12.74%, and 13.55% for pristine, BF-S, BF-M, and BF-L DPP-DTT films, respectively, implying that BF modification did not significantly alter the self-assembly behavior of DPP-DTT. We speculate that the "polymer-bag" effect allows a sufficient self-assembly time for the polymer semiconductor, even in the presence of water droplets. Nonetheless, the FET behavior of BF-modified DPP-DTT OFETs was inferior when compared to that of pristine DPP-DTT. As shown in Figure 3.1i, charge carrier mobility decreases from 0.072 of pristine to 0.050 of BF-L, 0.064 of BF-M and 0.065 cm^2 V^{-1} s^{-1} of BF-S. Similarly, V_{th} also shifted in a negative direction from –0.3 V for the pristine film to –8.41 V for BF-S, –12.1 V for BF-M, and –13.1 V for BF-L. Because the plots of $I_{DS}^{0.5}$ (drain-source current) versus V_{GS} (gate voltage) show excellent linearity, we could calculate

trap density variation as a result of BF-modification using the equation $\Delta N_{tr} = \frac{C_i \Delta V_{th}}{e}$, where C_i is the capacitance of the dielectric layer.[40] The calculated trap density variation for pristine OFET was 1.77×10^{12},
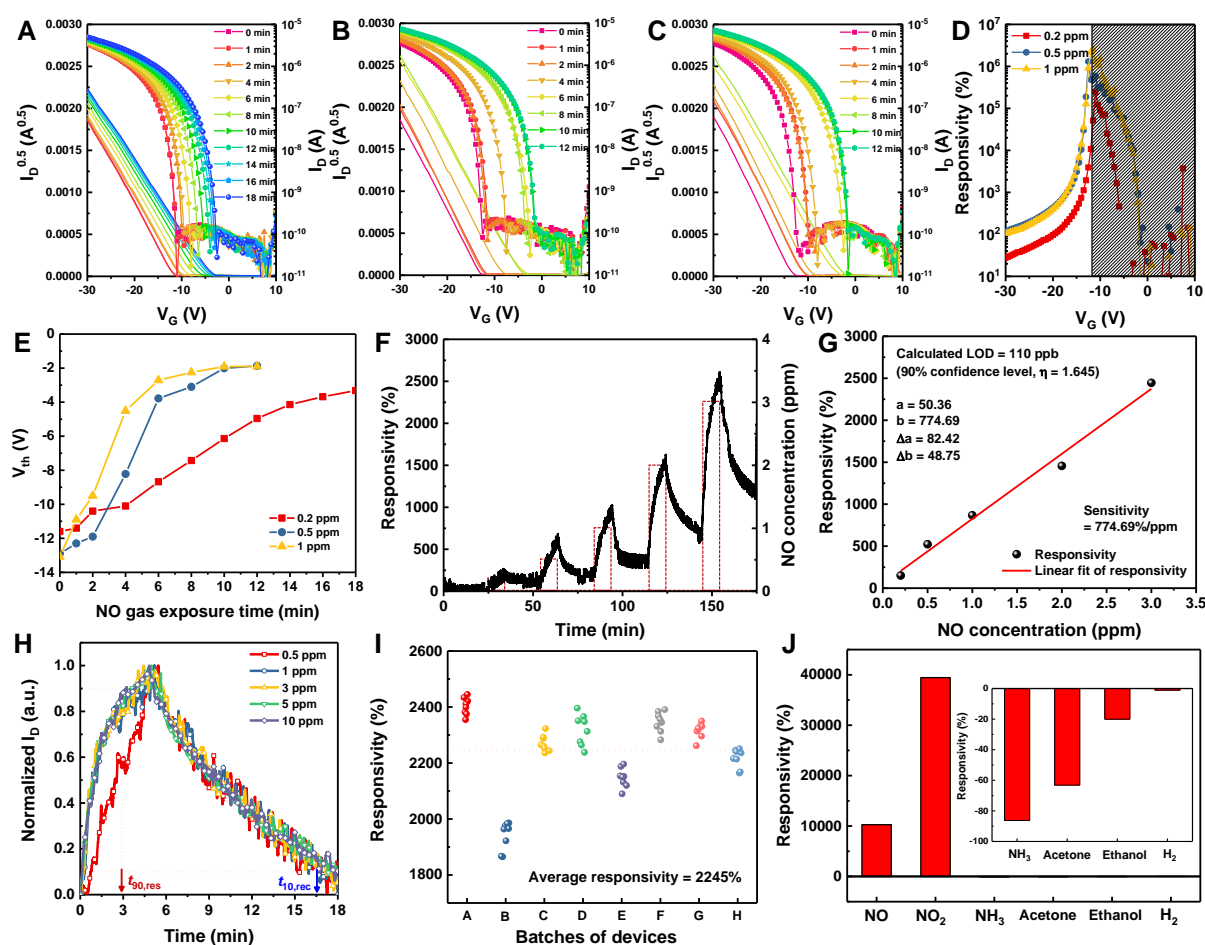
2.58×10^{12} and 2.80×10^{12} cm$^{−2}$ for BF-S, BF-M and BF-L; these values imply that the number of trap states increases as pore size increases. This result can be ascribed to larger pore boundary areas in the order of BF-L > BF-M > BF-S, as the pore boundary at which π-conjugation is physically terminated acts as a charge scattering center. Nonetheless, it is worthwhile to note that the overall OFET performance of BF-modified DPP-DTT was only slightly lesser than that of the pristine OFET and is higher than that of most previously reported OFET gas sensors. The responsivity values of BF-S, BF-M, and BF-L DPP-DTT are summarized in Figure 3.1j. The maximum responsivity of 10274% was observed for BF-M against 10 ppm NO, which is the highest value reported thus far for organic NO sensors and this responsivity is comparable to that of metal oxides.
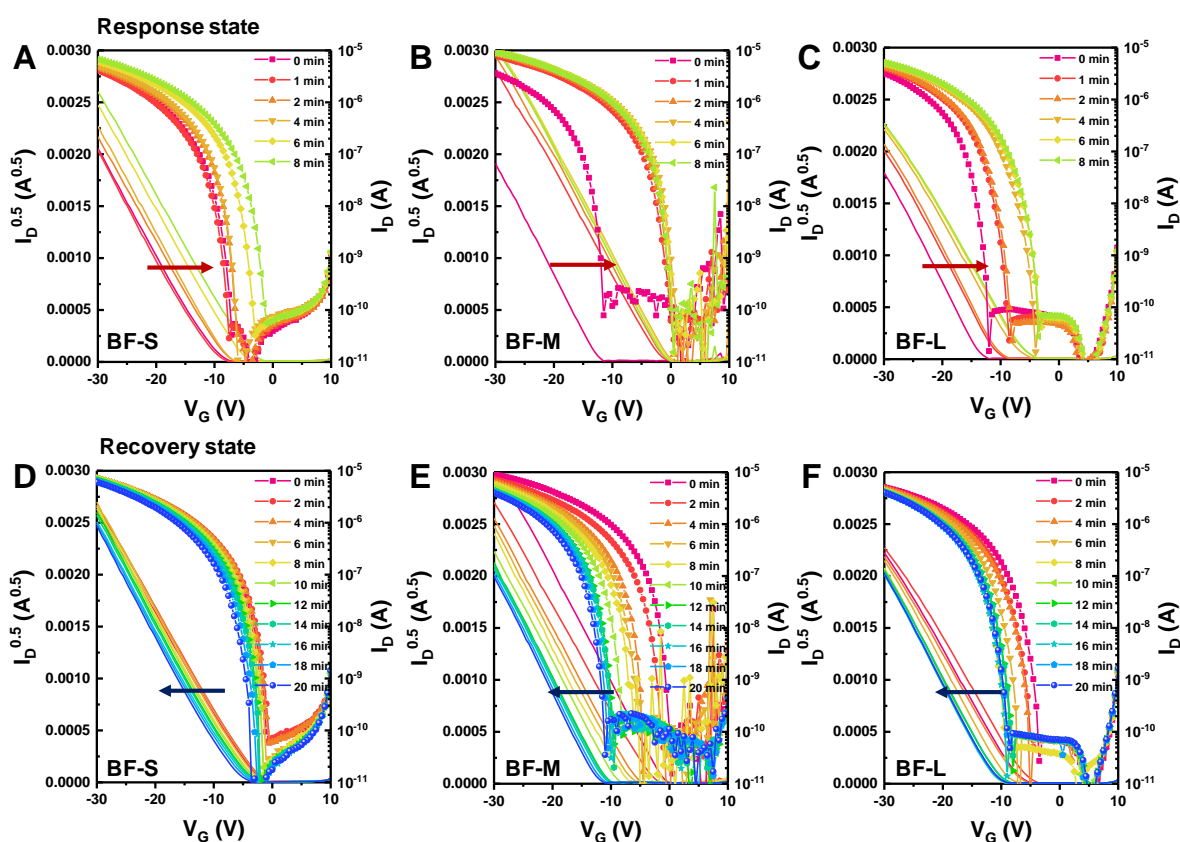
Figure 3.2 Transfer curves of (a) BF-S, (b) BF-M, and (c) BF-L at different time periods after exposure to 10 ppm NO. Recovery states of (d) BF-S, (e) BF-M, and (f) BF-L under N$_2$ purging.

Figure 3.2 summarizes time-dependent BF-S, BF-M, and BF-L DPP-DTT OFET sensor behaviors when exposed to 10 ppm NO. In the case of BF-S, a gradual positive shift is observed in the transfer curve up to 8 min of NO exposure (10 ppm) with a maximum ΔV_{th} of ~+8 V. Recovery upon N$_2$ exposure, however, was much slower with a ΔV_{th} of only –5 V even after 20 min. BF-M exhibited a far better sensing behavior with a prompt positive shift in the transfer curve with a ΔV_{th} of ~+10 V after only 1 min of NO exposure (10 ppm),

followed by a rapid and full recovery after 12 min. BF-L exhibited marginal sensing behavior with slower response and recovery when compared to BF-M, but its performance was better than that of BF-S. This implies that a pore size of ~750 nm is optimal for gas sensing in the case of BF modification of polymer semiconductors, especially for fast response and recovery. In each case, the gas exposure time and recovery time were maintained at 8 min and 20 min, respectively. Apparently low gas-reactivity of BF-S can be ascribed to the fact that its pores do not touch the dielectric surface, which limits gas exposure area of the polymer semiconductor. Relatively worse performance of BF-L compared to BF-M can be related with its too large grain boundary area, which weakens signal transport efficiency, as described in the OFET part.

Figure 3.3 Changes in the transfer curves at NO gas concentrations of (a) 0.2, (b) 0.5 and (c) 1 ppm, respectively. (d) Responsivities at various NO gas concentrations calculated from transfer curves corresponding to N_2 and NO gas exposure. The shaded region indicates a V_{GS} below V_{th}. (e) Threshold voltage shift with gas exposure time at various NO concentrations. (f) Transient response at 0.2–3 ppm NO at $V_{GS} = -15$ V and $V_{DS} = -30$ V. (g) Corresponding its responsivity and calculation of its sensitivity and LOD. (h) Normalized response at NO concentrations of 0.5–10 ppm. (i) Responsivity distribution upon exposure of 64 independently fabricated devices

- 46 -

to 3 ppm NO. (j) Responsivity of the sensor to upon exposure to different gases (concentration below 10 ppm). The bias condition is the same as that used for transient response measurements.

Figure 3.3 illustrates variations occurring in the ΔV_{th} of BF-M upon exposure to NO of various concentrations. It can be inferred from this plot that BF-M responds to NO very efficiently, even at concentrations as low as 200 ppb. The transient response of I_{DS} of BF-M OFET in a low NO concentration regime (from 0.2 to 3 ppm) at V_{GS} = –15 V and V_{DS} = –30 V is illustrated in Figure 3.3f. I_{DS} increases linearly with an increase in NO concentration and the OFET exhibited fast response with a recovery time of less than 12 min, which is fast enough for practical applications. Transient responsivity of the BF-M OFET was 150.3%, 522.9%, 867.6%, 1455.9%, and 2445.7% at NO concentrations of 0.2, 0.5, 1, 2, and 3 ppm, respectively. Sensitivity values extracted by fitting the measured responsivity values as a function of NO concentration are also summarized in Figure 3.3g; the highest value observed here, 774.69%/ppm, is the highest ever reported sensitivity for organic sensors (Table S1). Owing to manufacturing-imposed limitations of the test equipment, the lowest possible NO concentration that could be measured was 200 ppb. At this concentration, the responsivity was still as high as 150.3%. To estimate the limit of detection (LOD) for NO, we used the following equation
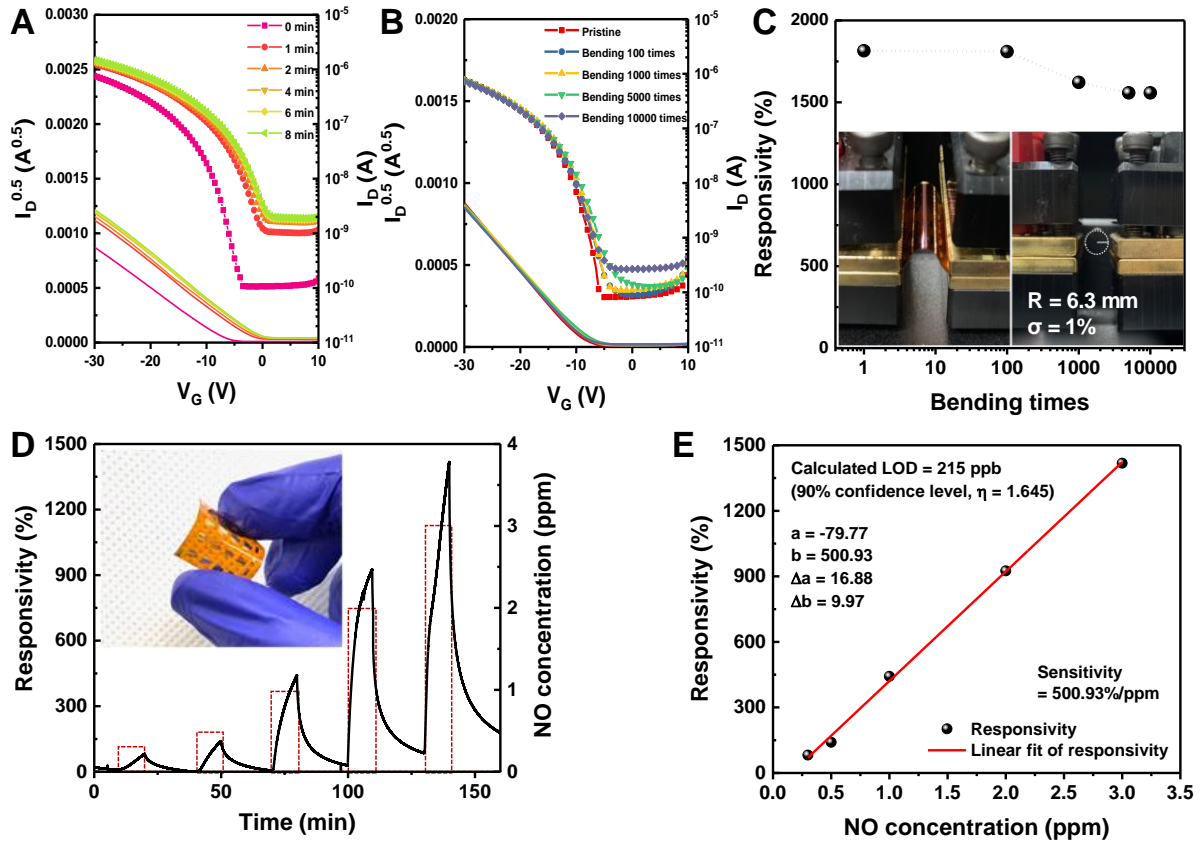
$$Y_{LOD} = \frac{-a \times b + \sqrt{a^2 \times b^2 - (b^2 - \eta^2 \times \Delta b^2)(a^2 - \eta^2 \times \Delta a^2)}}{b^2 - \eta^2 \times \Delta b^2}$$

(2)

where a, b, Δa, and Δb are parameters extracted from Figure 3.3g and η was assumed to be 1.645, which corresponds to a confidence interval level of 90%.[14,30,41] The estimated LOD was 110 ppb, which is the lowest value reported thus far for NO sensors based on either resistor or FET architectures.

Another notable advantage of this NO sensor platform is that both the response and recovery time are fast. Here, we employ the parameters $t_{90,res}$ and $t_{10,rec}$ to characterize the response and recovery time, respectively; $t_{90,res}$ is defined as the time required to reach 90% of ΔI in the response stage and $t_{10,rec}$ is defined as the time required for the current to go back to a level of $(I_0 + 10\% \times \Delta I)$ in the recovery stage.[23] Figure 3.3h illustrates the normalized transient responses of the BF-M platform at various NO concentrations. In the high concentration regime (over 10 ppm), $t_{90,res}$ and $t_{10,rec}$ were recorded as 174 s and 693 s, respectively, while a slightly longer $t_{90,res}$ of 267 s was recorded at 0.5 ppm. These response/recovery times are at least ~45%/~65% shorter than those of previously reported organic NO gas sensors.[32] Note that the time weighted average (TWA) value of NO exposure is up to 25 ppm. Human exposure to NO beyond the stated TWA can cause eye irritation and res-

piratory problems, which means that our sensor platform can previously/immediately alert when an environment becomes unsafe and precautions should be taken.[42]

For practical applications of the BF-OFET sensor platform, reproducibility is important. To evaluate device-to-device reliability, we conducted statistical analysis on 64 independently fabricated devices in 8 different batches with the same fabrication conditions (BF-M). Responsivity distribution at a NO concentration of 3 ppm is shown in Figure 3.3i. Approximately 71.8% of the devices exhibited a responsivity of more than 2200% (average responsivity of 2245% ± 141%), thus indicating the high reproducibility of BF-OFET gas sensors. Another important parameter to be considered for the practical application of a sensor is its selectivity towards specific gases. To evaluate the selectivity, BF-OFETs were exposed to various gas analytes including strongly oxidizing NO/NO_2, reducing NH_3, and VOCs such as ethanol/acetone; the resulting transfer curves were analyzed. At a gas concentration of 10 ppm, the responsivity of BF-OFET against different gas analytes was as shown in Figure 3.3j. Depending on the oxidizing/reducing nature of the tested gas analytes, a clear trend was observed. As a strongly oxidizing analyte, NO_2 resulted in the largest current modulation in a positive direction, with a responsivity of ~39448%, which is 3.8 times higher than that observed in the case of less oxidizing analyte, NO. Note that the obtained responsivity of 39448% against NO_2 is comparable to the recently reported high-performance of organic small molecule NO_2 sensors.[14,23] Reducing NH_3 resulted in a decrease in drain current, with a responsivity of –86.3%. In the case of less polar VOCs, both ethanol and acetone resulted in only a slight decrease in drain current with responsivities of –63.2% and –20.0%, respectively, owing to their weak oxidizing nature. Therefore, it can be concluded that the DPP-DTT BF-OFET is very selective to strong oxidizing/reducing gas analytes. Here, two points should be noted. 1) Oxidizing versus reducing analytes can be distinguished based on their different polarity of responsivity and 2) polar analytes versus VOCs can be distinguished based on the magnitude of responsivity.

Figure 3.4 (a) Changes in the transfer curves of flexible sensors upon exposure to 10 ppm NO. (b) Transfer curves after bending the sensor (radius: 6.3 mm, strain: 1%) for 0–10000 times. (c) Responsivity changes after bending the sensor for 0–10000 times and exposing it to 3 ppm NO. The photo shows the actual bending test and radius of curvature. (d) Transient response of the flexible sensor upon exposure to 0.5–3 ppm NO at $V_{GS}= -8$ V and $V_{DS}= -30$ V. The inset image is actual flexible device. (e) Corresponding its responsivity and calculation of its sensitivity and LOD. The bias condition is the same as that used for transient response measurements.

The unique advantage of polymer OFET gas sensors is their mechanical flexibility and thus flexible OFETs were fabricated from BF-molded polymer semiconductors. In this case, patterned Ag was used as the gate electrode on a polyimide substrate and poly(4-vinylphenol) (PVP) was used as the dielectric layer. All other fabrication steps were the same, with BF-modified DPP-DTT as the channel layer and Au as the source-drain electrode. To demonstrate the stable operation of flexible DPP-DTT BF-OFET gas sensors under bending stress, sensor properties were analyzed in terms of the bending radius. Figure 3.4a shows the transfer curves of the fabricated BF-OFET gas sensor under NO exposure (10 ppm). Similar to a Si^{++}/SiO_2 gate dielectric device, an apparent positive shift was observed in the transfer curves of BF-OFET upon NO exposure and in recovery curves upon N_2 exposure, but with a lower sensitivity and slower response/recovery behavior. We speculate that

the weak performance of the flexible device compared to the Si^{++}/SiO_2 gate dielectric device is related to interface trap states between the dielectric layer and semiconductor layer formed by the gate dielectric solution process. Nonetheless, the observed sensitivity of 500.93%/ppm against NO is the highest value reported thus far for flexible organic gas sensors. The transfer curves of the flexible devices change only slightly after bending as shown in Figure 3.4b. As shown in Figure 3.4c, the responsivity of the DPP-DTT BF-OFET gas sensor against 3 ppm NO was continuously measured while performing 10,000 bending cycles at a strain of 1%. The strain in DPP-DTT BF-OFET was calculated using the following equation

$$\text{Strain}(\sigma) = \frac{D}{2R}$$

(3)

where D is the total thickness of the device and R is the bending radius.[43] During the bending test, the responsivity of DPP-DTT BF-OFET was remarkably stable, with a responsivity degradation of only 14.2% after 10,000 bending cycles.

V. Conclusion

In summary, we demonstrated highly sensitive and selective flexible polymer transistor gas sensors, mainly targeted at NO_x. To obtain high-performance polymer transistor gas sensors, we selected the DPP-DTT polymer, which exhibits efficient dipole-dipole interaction with gas molecules. In addition, we employed the BF molding method to maximize gas-polymer interfacial area and thus sensitivity against gas analytes, while preserving the inherent signal transport characteristics of the semiconductor. The optimized BF-OFET with an average pore size of 750 nm resulted in a maximum responsivity of over 104%, sensitivity greater than 774%/ppm, and LOD of 110 ppb against NO. Furthermore, the sensor exhibited a short response/recovery time suitable for practical applications and a high reproducibility. Finally, we fabricated flexible BF-OFETs on plastic substrates and these devices exhibited outstanding bending stability. We believe that this facile BF molding strategy is a breakthrough in the field of polymer semiconductor gas sensors, whose morphology is generally difficult to control unlike in the case of small molecule semiconductors.

V. References

[1]   Fahad, H.M., Shiraki, H., Amani, M., Zhang, C., Hebbar, V.S., Gao, W., Ota, H., Hettick, M., Kiriya, D., Chen, Y.Z. and Chueh, Y.L., 2017. Room temperature multiplexed gas sensing using chemical-sensitive 3.5-nm-thin silicon transistors. Science advances, 3(3), p.e1602557.

[2]   Lee, M.Y., Lee, H.R., Park, C.H., Han, S.G. and Oh, J.H., 2018. Organic transistor-based chemical sensors for wearable bioelectronics. Accounts of chemical research, 51(11), pp.2829-2838.

[3]   Han, S.T., Peng, H., Sun, Q., Venkatesh, S., Chung, K.S., Lau, S.C., Zhou, Y. and Roy, V.A.L., 2017. An overview of the development of flexible sensors. Advanced Materials, 29(33), p.1700375.

[4]   Zhang, C., Chen, P. and Hu, W., 2015. Organic field-effect transistor-based gas sensors. Chemical Society Reviews, 44(8), pp.2087-2107.

[5]   Zang, Y., Huang, D., Di, C.A. and Zhu, D., 2016. Device engineered organic transistors for flexible sensing applications. Advanced Materials, 28(22), pp.4549-4555.

[6]   Ma, Z., Chen, P., Cheng, W., Yan, K., Pan, L., Shi, Y. and Yu, G., 2018. Highly sensitive, printable nanostructured conductive polymer wireless sensor for food spoilage detection. Nano letters, 18(7), pp.4570-4575.

[7]   Stanford, M.G., Yang, K., Chyan, Y., Kittrell, C. and Tour, J.M., 2019. Laser-induced graphene for flexible and embeddable gas sensors. ACS nano, 13(3), pp.3474-3482.

[8]   Zhang, F., Qu, G., Mohammadi, E., Mei, J. and Diao, Y., 2017. Solution-Processed Nanoporous Organic Semiconductor Thin Films: Toward Health and Environmental Monitoring of Volatile Markers. Advanced Functional Materials, 27(23), p.1701117.

[9]   Khim, D., Ryu, G.S., Park, W.T., Kim, H., Lee, M. and Noh, Y.Y., 2016. Precisely controlled ultrathin conjugated polymer films for large area transparent transistors and highly sensitive chemical sensors. Advanced Materials, 28(14), pp.2752-2759.

[10]   Urasinska-Wojcik, B., Vincent, T.A., Chowdhury, M.F. and Gardner, J.W., 2017. Ultrasensitive WO3 gas sensors for NO2 detection in air and low oxygen environment. Sensors and Actuators B: Chemical, 239, pp.1051-1059.

[11]   Shendage, S.S., Patil, V.L., Vanalakar, S.A., Patil, S.P., Harale, N.S., Bhosale, J.L., Kim, J.H. and Patil, P.S., 2017. Sensitive and selective NO2 gas sensor based on WO3 nanoplates. Sensors and Actuators B: Chemical, 240, pp.426-433.

[12]   Chatterjee, S.G., Chatterjee, S., Ray, A.K. and Chakraborty, A.K., 2015. Graphene–metal oxide nanohybrids for toxic gas sensor: a review. Sensors and Actuators B: Chemical, 221, pp.1170-1181.

[13]   Long, H., Harley-Trochimczyk, A., Pham, T., Tang, Z., Shi, T., Zettl, A., Carraro, C., Worsley, M.A. and Maboudian, R., 2016. High surface area MoS2/graphene hybrid aerogel for ultrasensitive NO2 detection. Advanced Functional Materials, 26(28), pp.5158-5165.

[14]   Huang, W., Zhuang, X., Melkonyan, F.S., Wang, B., Zeng, L., Wang, G., Han, S., Bedzyk, M.J., Yu, J., Marks, T.J. and Facchetti, A., 2017. UV–Ozone interfacial modification in organic transistors for

high-sensitivity NO2 detection. Advanced Materials, 29(31), p.1701706.

[15]   Lu, J., Liu, D., Zhou, J., Chu, Y., Chen, Y., Wu, X. and Huang, J., 2017. Porous organic field-effect transistors for enhanced chemical sensing performances. Advanced Functional Materials, 27(20), p.1700018.

[16]   Yu, S.Y., Tung, T.W., Yang, H.Y., Chen, G.Y., Shih, C.C., Lee, Y.C., Chen, C.C., Zan, H.W., Meng, H.F., Lu, C.J. and Wang, C.L., 2019. A Versatile Method to Enhance the Operational Current of Air-Stable Organic Gas Sensor for Monitoring of Breath Ammonia in Hemodialysis Patients. ACS sensors, 4(4), pp.1023-1031.

[17]   Lu, C.F., Shih, C.W., Chen, C.A., Chin, A. and Su, W.F., 2018. Tuning the Morphology of Isoindigo Donor–Acceptor Polymer Film for High Sensitivity Ammonia Sensor. Advanced Functional Materials, 28(40), p.1803145.

[18]   Yu, S.H., Cho, J., Sim, K.M., Ha, J.U. and Chung, D.S., 2016. Morphology-driven high-performance polymer transistor-based ammonia gas sensor. ACS applied materials & interfaces, 8(10), pp.6570-6576.

[19]   Han, S., Zhuang, X., Shi, W., Yang, X., Li, L. and Yu, J., 2016. Poly (3-hexylthiophene)/polystyrene (P3HT/PS) blends based organic field-effect transistor ammonia gas sensor. Sensors and Actuators B: Chemical, 225, pp.10-15.

[20]   Chuang, M.Y., Lin, Y.T., Tung, T.W., Chang, L.Y., Zan, H.W., Meng, H.F., Lu, C.J. and Tao, Y.T., 2018. Room-temperature-operated organic-based acetone gas sensor for breath analysis. Sensors and Actuators B: Chemical, 260, pp.593-600.

[21]   Peng, B., Huang, S., Zhou, Z. and Chan, P.K.L., 2017. Solution-Processed Monolayer Organic Crystals for High-Performance Field-Effect Transistors and Ultrasensitive Gas Sensors. Advanced Functional Materials, 27(29), p.1700999.

[22]   Sizov, A.S., Trul, A.A., Chekusova, V., Borshchev, O.V., Vasiliev, A.A., Agina, E.V. and Ponomarenko, S.A., 2018. Highly Sensitive Air-Stable Easily Processable Gas Sensors Based on Langmuir–Schaefer Monolayer Organic Field-Effect Transistors for Multiparametric H2S and NH3 Real-Time Detection. ACS applied materials & interfaces, 10(50), pp.43831-43841.

[23]   Wang, Z., Huang, L., Zhu, X., Zhou, X. and Chi, L., 2017. An Ultrasensitive Organic Semiconductor NO2 Sensor Based on Crystalline TIPS-Pentacene Films. Advanced Materials, 29(38), p.1703192.

[24]   Yang, Y., Liu, Z., Chen, L., Yao, J., Lin, G., Zhang, X., Zhang, G. and Zhang, D., 2019. Conjugated Semiconducting Polymer with Thymine Groups in the Side Chains: Charge Mobility Enhancement and Application for Selective Field-Effect Transistor Sensors toward CO and H2S. Chemistry of Materials, 31(5), pp.1800-1807.

[25]   Nketia-Yawson, B., Jung, A.R., Noh, Y., Ryu, G.S., Tabi, G.D., Lee, K.K., Kim, B. and Noh, Y.Y., 2017. Highly sensitive flexible NH3 sensors based on printed organic transistors with fluorinated conjugated polymers. ACS applied materials & interfaces, 9(8), pp.7322-7330.

[26]   Yang, Y., Zhang, G., Luo, H., Yao, J., Liu, Z. and Zhang, D., 2016. Highly sensitive thin-film field-effect transistor sensor for ammonia with the DPP-bithiophene conjugated polymer entailing thermally cleavable tert-butoxy groups in the side chains. ACS applied materials & interfaces, 8(6), pp.3635-3643.

[27]   Gusain, A., Joshi, N.J., Varde, P.V. and Aswal, D.K., 2017. Flexible NO gas sensor based on conducting   polymer   poly   [N-9′-heptadecanyl-2,   7-carbazole-alt-5,   5-(4′,   7′-di-2-thienyl-2′,   1′,   3′-

benzothiadiazole)](PCDTBT). Sensors and Actuators B: Chemical, 239, pp.734-745.

[28]   Lee, B., 1991. Highlights of the clean air act amendments off 1990. Journal of the Air & Waste Management Association, 41(1), pp.16-19..

[29]   Lewis Sr, R.J., 2008. Hazardous chemicals desk reference. John Wiley & Sons.

[30]   Mirza, M., Wang, J., Wang, L., He, J. and Jiang, C., 2015. Response enhancement mechanism of NO2 gas sensing in ultrathin pentacene field-effect transistors. Organic Electronics, 24, pp.96-100.

[31]   Andringa, A.M., Spijkman, M.J., Smits, E.C., Mathijssen, S.G., van Hal, P.A., Setayesh, S., Willard, N.P., Borshchev, O.V., Ponomarenko, S.A., Blom, P.W. and de Leeuw, D.M., 2010. Gas sensing with self-assembled monolayer field-effect transistors. Organic Electronics, 11(5), pp.895-898.

[32]   Marinelli, F., Dell'Aquila, A., Torsi, L., Tey, J., Suranna, G.P., Mastrorilli, P., Romanazzi, G., Nobile, C.F., Mhaisalkar, S.G., Cioffi, N. and Palmisano, F., 2009. An organic field effect transistor as a selective NOx sensor operated at room temperature. Sensors and Actuators B: Chemical, 140(2), pp.445-450.

[33]   Bunz, U.H.F., 2006. Breath figures as a dynamic templating method for polymers and nanomaterials. Advanced Materials, 18(8), pp.973-989.

[34]   Munoz-Bonilla, A., Fernández-García, M. and Rodríguez-Hernández, J., 2014. Towards hierarchically ordered functional porous polymeric surfaces prepared by the breath figures approach. Progress in Polymer Science, 39(3), pp.510-554.

[35]   Munoz-Bonilla, A., Ibarboure, E., Papon, E. and Rodriguez-Hernandez, J., 2009. Self-organized hierarchical structures in polymer surfaces: self-assembled nanostructures within breath figures. Langmuir, 25(11), pp.6493-6499.

[36]   Routh, P.K., Nykypanchuk, D., Venkatesh, T.A. and Cotlet, M., 2015. Long Range Self-Assembly of Polythiophene Breath Figures: Optical and Morphological Characterization. Advanced Functional Materials, 25(37), pp.5902-5909.

[37]   Rivnay, J., Mannsfeld, S.C., Miller, C.E., Salleo, A. and Toney, M.F., 2012. Quantitative determination of organic semiconductor microstructure from the molecular to device scale. Chemical reviews, 112(10), pp.5488-5519.

[38]   Baker, J.L., Jimison, L.H., Mannsfeld, S., Volkman, S., Yin, S., Subramanian, V., Salleo, A., Alivisatos, A.P. and Toney, M.F., 2010. Quantification of thin film crystallographic orientation using X-ray diffraction with an area detector. Langmuir, 26(11), pp.9146-9151.

[39]   Noriega, R., Rivnay, J., Vandewal, K., Koch, F.P., Stingelin, N., Smith, P., Toney, M.F. and Salleo, A., 2013. A general relationship between disorder, aggregation and charge transport in conjugated polymers. Nature materials, 12(11), pp.1038-1044.

[40]   Podzorov, V., Menard, E., Borissov, A., Kiryukhin, V., Rogers, J.A. and Gershenson, M.E., 2004. Intrinsic charge transport on the surface of organic semiconductors. Physical review letters, 93(8), p.086602.

[41]   Zheng, H., Ramalingam, B., Korampally, V. and Gangopadhyay, S., 2013. Large sensitivity enhancement in semiconducting organic field effect transistor sensors through incorporation of ultra-fine platinum nanoparticles. Applied Physics Letters, 103(19), p.210_1.

[42]   Barsan, M.E., 2007. NIOSH pocket guide to chemical hazards..

[43]   Lai, H.C., Pei, Z., Jian, J.R. and Tzeng, B.J., 2014. Alumina nanoparticle/polymer nanocomposite dielectric for flexible amorphous indium-gallium-zinc oxide thin film transistors on plastic substrate with supe-

rior stability. Applied Physics Letters, 105(3), p.033510.

[44]   Lee, I.Y., Park, H.Y., Park, J.H., Yoo, G., Lim, M.H., Park, J., Rathi, S., Jung, W.S., Kim, J., Kim, S.W. and Roh, Y., 2014. Poly-4-vinylphenol and poly (melamine-co-formaldehyde)-based graphene passivation method for flexible, wearable and transparent electronics. Nanoscale, 6(7), pp.3830-3836.

[45]   Lim, S.C., Kim, S.H., Koo, J.B., Lee, J.H., Ku, C.H., Yang, Y.S. and Zyung, T., 2007. Hysteresis of pentacene thin-film transistors and inverters with cross-linked poly (4-vinylphenol) gate dielectrics. Applied physics letters, 90(17), p.173512.

[46]   Haerri, H.P., Macé, T., Waldén, J., Pascale, C., Niederhauser, B., Wirtz, K., Stovcik, V., Sutour, C., Couette, J. and Waldén, T., 2017. Dilution and permeation standards for the generation of NO, NO2 and SO2 calibration gas mixtures. Measurement Science and Technology, 28(3), p.035801.

요 약 문

유기 반도체를 이용한 유연 전자 소자 개발

본 논문은 유기 반도체를 이용한 유연 소자 개발 방법들을 제시한다: (1) 고분자 반도체의 공액 길이에 따른 전하 이동 영향, (2) 수분산 유기 반도체 콜로이드 합성 및 이를 이용한 소자 개발, (3) breath-figure 패턴 몰딩법을 이용한 센서 개발.

디케토피롤로피롤(diketopyrrolopyrrole) 전자 주개-받개 구조의 공중합체 반도체의 전하 운반체 이동성을 향상시키기 위해, 주개 구조의 길이는 비닐렌 단위체를 사용하여 제어된 채 결정 구조 및 전하 수송에 미치는 영향을 체계적으로 연구한다. 티오펜 단위체 사이에 2 개의 비닐렌 결합을 갖는 P29-DPP-TBT를 합성하고 단일 비닐렌 결합을 갖는 P29-DPP-TVT와 비교한다. 분자 이론 계산을 통하여 P29-DPP-TVT와 비교하여 P29-DPP-TBT의 향상된 백본 평면성을 예측하고, 자외선-가시광선 흡광 스펙트럼과 라만 스펙트럼을 이용하여 추출된 자유 엑시톤 대역폭이 증가함에 따라 P29-DPP-TBT의 공액 길이가 길어짐을 증명한다. 2 차원 X- 선 회절 분석법을 이용하여, P29-DPP-TVT보다 P29-DPP-TBT에서 결정성이 뛰어남을 확인하였다. 추가적으로, X- 선 흡수 미세 구조 분광법에서 P29-DPP-TBT의 경우에 고분자 백본이 더 많은 에지-온 구조로 형성됨을 보여준다. 전하이동도의 온도 의존성을 측정함으로써, 전하 호핑을 위한 활성화 에너지는 P29-DPP-TVT보다 P29-DPP-TBT에 대해 더 낮은 것으로 밝혀졌다. 종합적으로, 이들 결과는 공중합체 고분자 반도체의 연장된 π- 공액 전자 주개 부분의 치환이 보다 평면적인 골격 구조를 생성할 수 있고, 이에 따라 보다 완전한 결정질 구조 및 향상된 전하 수송 거동을 가능하게 하여 분자간 상호 작용을 향상시킬 수 있음을 의미한다.

고분자 합성 측면에 있어 수성 콜로이드의 박막화 동안 응축 현상을 향상시켜서, 고분자 반도체의 얇고 균일하며 연속적인 박막 형태가 실현될 수 있음을 입증하였다. 콜로이드에 대한 이론적 연구로, 크기가 작고 균일한 콜로이드 입자가 콜로이드 입자 사이의 공핍 접촉 에너지를 최소화하고 따라서 응축을 향상시키는 데 필수적이라는 것이 밝혀졌다. 따라서, 새롭게 합성된 공중합체 고분자 반도체는 계면활성제와의 분자 친화성이 향상되도록 설계되어, 유기상으로부터

수상으로 공중합체 고분자 반도체의 상 전이가 미니-에멀전 합성 동안 보다 효율적으로 진행될 수 있다. 이는 통상적인 전자 주개-받개 구조의 공중합체 고분자 반도체의 알킬 체인 그룹의 분지형 C 원자에 Si 원자를 치환함으로써 가능하게 하였다. 이러한 화학적 변형은 소수성 알킬 체인의 부피를 증가시키고 따라서 더 높은 용해도 및 더 높은 소수성을 가능하게 하며, 이는 모두 공중합체 고분자 반도체와 계면활성제 사이의 분자 친화도를 향상시키는 것과 밀접한 관련이 있다. 결과적으로, 수계 콜로이드로 제조된 유기 전계 효과 트랜지스터의 성능은 유기 용매의 경우와 유사한 수준으로 개선될 수 있음을 입증하였다. 더불어 작고 균일한 수성 콜로이드 입자로 인해 박막 트랜지스터 성능의 재현성이 크게 향상된다.

특정 가스 분석 물질에 대한 높은 반응성과 높은 신호 전송 효율을 모두 갖춘 고분자 반도체 박막 모폴로지를 구현함으로써, 고성능의 유연한 NOₓ 가스 센서를 실현하였다. 고분자 반도체의 Breath-Figure (BF) 몰딩은 유기 전계 효과 트랜지스터 (OFET)의 높은 전하 캐리어 이동 특성을 유지하면서 고분자 박막에서 미세한 크기의 나노 다공성 표면 개질을 가능하게 하였다. 전자 주개-받개 구조의 공중합체 기반의 최적화된 BF-OFET는 최대 10^4 % 이상의 반응성과, 774% / ppm의 감도 및 NO에 대한 110 ppb의 검출 한계 (LOD)를 나타낸다. 0.2 ~ 10ppm의 NO 농도에서 측정시에 BF-OFET 가스 센서는 100 ~ 300 초의 응답 시간을 나타내며 이는 실제 응용 소자로 쓰일 수 있는 수준이다. 또한, BF-OFET는 64 개의 독립적으로 제조된 소자에 대한 통계 분석에 의해 확인 된 바와 같이 높은 재현성을 나타낸다. NOₓ 가스에 대한 선택성은 BF-OFET의 감지 능력을 다른 환원 가스 및 휘발성 유기 화합물과 비교하여 측정하였다. 최종적으로 플라스틱 기판과 접합된 유연한 BF-OFET을 구현하였으며 이 소자는 1% 변형률에서 10,000 회 굽힘 주기 후 14.2%의 응답성 저하를 보였으며, 500 % / ppm의 감도와 215ppb의 LOD를 나타냈다.